Influence of artificial roughness parametric variation on thermal performance of solar thermal collector: An experimental study, response surface analysis and ANN modelling

Raj Kumar [a], Rahul Nadda [b], Sushil Kumar [c,*], Abdul Razak [d], Mohsen Sharifpur [e,f,*], Hikmet S. Aybar [g,h], C Ahamed Saleel [i], Asif Afzal [d,j,*]

[a] Faculty of Engineering and Technology, Shoolini University, Solan H.P. 173229, India
[b] Department of Biomedical Engineering, Indian Institute of Technology Ropar, Punjab 140001, India
[c] Department of Physics, Hansraj College, University of Delhi, India
[d] Department of Mechanical Engineering, P. A. College of Engineering (Affiliated to Visvesvaraya Technological University, Belagavi), Mangaluru 574153, India
[e] Department of Mechanical and Aeronautical Engineering, University of Pretoria, Pretoria 0002, South Africa
[f] Department of Medical Research, China Medical University Hospital, China Medical University, Taichung, Taiwan
[g] Laser Applications Research Group, Ton Duc Thang University, Ho Chi Minh City, Vietnam
[h] Faculty of Electrical and Electronics Engineering, Ton Duc Thang University, Ho Chi Minh City, Vietnam
[i] Department of Mechanical Engineering, College of Engineering, King Khalid University, PO Box 394, Abha 61421, Saudi Arabia
[j] Department of Mechanical Engineering, School of Technology, Glocal University, Delhi-Yamunotri Marg, SH-57, Mirzapur Pole, Saharanpur District, Uttar Pradesh 247121, India

ARTICLE INFO

Keywords:
Heat transfer
Baffle width
Perforated baffles
Artificial Neural Network
Thermal hydraulic performance

ABSTRACT

The influence of the attack angle (α_a) of the perforated baffles on thermohydraulic performance (η_p) of a solar thermal collector (STC) has been investigated experimentally. The experimentations have been performed to obtain the Nusselt number (Nu_{rs}) and friction factor (f_{rs}) by varying Reynolds number (Re) from 5000 to 17,000 and α_a from 35° to 65°. The other geometrical parameters of angled perforated baffles are fixed in accordance with previous studies. The relative baffle height (H_B/H_D) , relative baffle pitch (P_B/H_B) , relative hole position (O_B/H_B) and open area ratio (β_0) are fixed at 0.50, 10, 0.266 and 12% respectively. The STC with roughened angled perforated baffles improves the Nu_{rs} and f_{rs} by 3.82 and 7.14 times respectively as compared to STC without baffles wall. The angled perforated baffles at α_a of 55° provides highest thermo-hydraulic performance at Re of 9000. A thermo-hydraulic performance of 1.94 is obtained for the array of designed parameters. The statistical correlations are established for the Nu_{rs} and f_{rs} by using experimental data. The correlations obtained for the Nu_{rs} and f_{rs} predict the experimental results within a variation of ±9.7% and ±5.0% respectively. Central Composite Design (CCD) of thermo-hydraulic performance parameters is carried for the surface response analysis. Modelling of thermal parameters using CCD and Artificial Neural Network (ANN) is done which predict them with good accuracy. The previously studies on STC roughened with various types of roughness show appreciable heat transfer enhancement but very few studies have utilized angled perforated baffles. As per author knowledge, a comprehensive study on the performance analysis of STC roughened with angled perforated baffles using different techniques is not available. The study become novel because in addition to the experimental examination of STC performance, correlations for Nu_{rs} and f_{rs} from experimental data are developed and modelling of thermal parameters using CCD and Artificial Neural Network (ANN) is also performed.

Introduction

The energy coming from the sun is the main resource for mankind and an unpolluted natural source of energy [1]. This energy can be converted into other forms which are used in various engineering applications. The solar thermal collector (STC) transforms solar energy into heat energy which finds applications in various areas such as domestic heating purposes and drying of agricultural products [2–5]. The heat transfer (HT) rate in STC is increased by employing different

* Corresponding authors at: Department of Physics, Hansraj College, University of Delhi, India (S. kumar).
E-mail addresses: sushil8207@gmail.com (S. Kumar), mohsen.sharifpur@up.ac.za (M. Sharifpur), asif.afzal86@gmail.com (A. Afzal).

Nomenclature

ANN	Artificial Neural Network
T_f	Average temperature of the air, (^{0}C)
H_B	Baffle height, (mm)
CCD	Central composite design
W_D/H_D	Channel aspect ratio, (dimensionless)
H_D	Channel height, (mm)
D_{hd}	Channel hydraulic diameter, (mm)
W_D	Channel width, (mm)
h_t	Convective heat transfer coefficient, (W/m^2K)
Δh_0	Difference of head in the manometer, (mm)
C_{d0}	Discharge coefficient, (dimensionless)
T_i	Entrance temperature of the air, ^{0}C
T_o	Exit temperature of the air, ^{0}C
f_{rs}	Friction factor with perforated angled baffles, (dimensionless)
f_{ss}	Friction factor without baffles, (dimensionless)
f	Friction factor, (dimensionless)
A_P	Heated plate surface area, mm^2
O_B	Hole position from baffle base, mm
L_V	Length of angled pattern baffle, mm
m_a	Mass flow rate of air, (kg/s)
V	Mean air velocity, (m/s)
T_p	Mean absorber plate temperature, (^{0}C)
Nu_{rs}	Nusselt number of perforated angled baffles surface, (dimensionless)
Nu_{ss}	Nusselt number of the surface without baffles, (dimensionless)
Nu	Nusselt number, (dimensionless)
A_o	Orifice area, mm^2
d_h	Perforated baffle hole diameter, mm
P_B	Pitch of baffle channel, (mm)
$(\Delta_p)_0$	Pressure drop across orifice plate, (Pa)
$(\Delta_p)_d$	Pressure drop across the test section, (Pa)
P_B/H_B	Relative baffle pitch ratio, (dimensionless)
O_B/H_B	Relative hole position, (dimensionless)
Re	Reynolds number of fluid, (dimensionless)
SAC	Solar air channel
SAH	Solar air heater
STC	Solar thermal collector
C_p	Specific heat of fluid (J/kgK)
L_t	Test section length, (mm)
k_a	Thermal conductivity of air, (W/mK)
TP	Thermal Performance
Q_u	Useful energy gain, (W)

Greek symbols

α_a	Angle of attack, ($^\circ$)
β_O	Open area ratio, (%)
β_R	Ratio of orifice meter to pipe diameter, (dimensionless)
ρ_a	Air density, (kg/m^3)
υ_a	Kinematic viscosity of air, (m^2/s)
η_p	Thermal hydraulic performance, (dimensionless)

artificial roughness (AR). One of the most efficient techniques of HT enhancement is artificial roughening of the absorber plate. The AR can be provided in terms of different shape and size such as ribs, winglets, dimple, and baffles. The AR parameters are usually indicated by dimensionless factors such as relative roughness height, relative roughness pitch, angle of attack, relative gap position, relative gap width, groove position and chamfer angle etc. The AR can be in the form of angled ribs or continuous or broken ribs, chamfered, circular, semi-circular, grooved section metal mesh, arc shaped and Multi V-shaped. The AR generates two flow separation regions, one on each side of the roughness element. The vortices cause the turbulence and hence HT and friction factor increase. Distinct efforts have been made by the researchers for HT rate improvement in STC using different AR on the absorber plate and energy storage medium [6]. Khargotra et al. [7] studied the influence of delta-winglets on the Nu and f in solar water heater. The parameters of the delta-winglets such as P_B/H_B , H_B/H_D , α_a and spacer length (SWH) were varied in the experimentation. They found 4.56 times higher Nu for SWH with delta winglets than that of smooth tube. A thermohydraulic performance of 2.62 is obtained for SWH with delta winglets. Khargotra et al. [8] examined the η_p of SWH using non-circular holes in perforated delta-winglets. The results show that the perforated delta-winglets with circularity of 0.86, P_B/H_B of 0.5, α_a of 450 and spacer length of 0 mm have optimum impact on Nu and f of the SWH. Singhy et al. [9] developed a novel concentrated photovoltaic thermal system (CPVT) with combination of Fresnel lens (FL) and convex lens (CL). IV characteristics of PV module without lens, with FL and together with FL/CL determined during analysis. The results show that the obtained efficiency of PVT system and standalone system were 53.7% and 47.61% respectively. Bhardwaj et al. [10] studied the thermal augmentation of an economically feasible and minimum cost forced convection solar dryer. The STC prepared with sensible heat storing medium to control the temperature variations. The assessment of individual element of the drying system was scrutinized based on energy and exergy analysis. Bhardwaj et al. [11] carried out experimental examination of an indirect solar dryer for drying chillies in the Western Himalayas. STC encompasses sensible and latent heat storage medium. The performance assessment of the STC has been analyzed based on thermal, physical, and quality attributes. Modified drying system provides improved quality of the dehydrated chillies in the form of colour, texture, and pungency. Kashyap et al. [12] carried out experimental analysis of the Archimedes Screw Turbine for its efficiency improvement. The authors concluded that the efficiency of the Archimedes Screw Turbine improved for screw angle ranges between 20° to 25° and stream rate less than 1.5 L/s. Bhatter et al. [13] investigated the impact of position of the baffles on η_p of rectangular duct SAH. The results pointed out that for 60 mm pitch among the baffles and 200 mm space of the first row from the inlet, the maximum value of thermo-hydraulic performance factor (THPF) of 0.9339 was achieved. Kumar et al. [14] examined HT characteristics in SAH having multi-V- type perforated baffles mounted on tested plate. In the proposed experiment, the relative baffle height of 0.6, pitch of 8.0, angle of attack 60°, relative hole position 0.42 & open area ratio of baffles of 12% was considered. The numerical analysis was obtained by using k-ε model of turbulence and investigation was conducted for optimum relative baffles width varying from 1.0 to 7.0. The obtained results concluded that the highest η_p was attained at relative baffles width of 5.0. The influence of the various baffle blockage ratio varied from 0.7 to 0.98 and effect of four baffle pitch spacing ratio (P_R) varied from 2 to 8 was investigated by Menasria et al. [15].

Hoonpong et al. [16] concentrated on the performance enhancement of the SAH integrated with V baffles attached on the absorber plate. In this work, the *Re* changed from 5300 to 22,600 and the effect of the three different baffles height (R_B) and three various relative pitch (R_P) on the TP was examined. The obtained outcomes concluded that highest thermal performance of 1.57 was achieved for R_B of 0.2 and R_P of 1.0. Laun et al. [17] presented the correlation for *Nu* and *f* from the

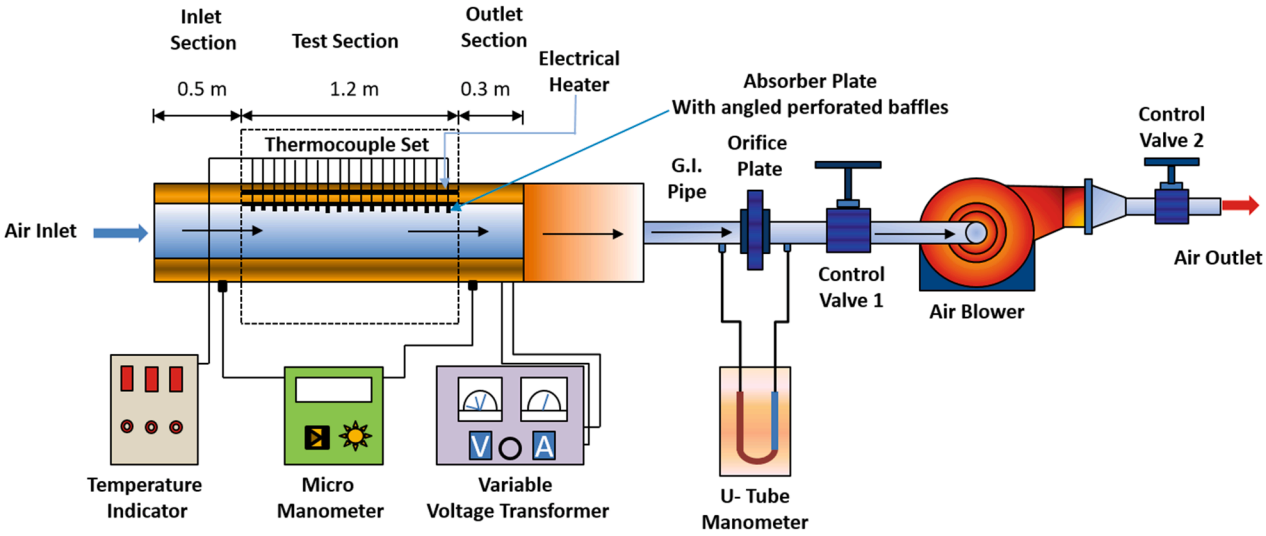

Fig. 1. Schematic diagram of experimental arrangement.

experimental data of SAC with inclined baffles. In this study, the inclination angle of baffles varied from 0° to 180°. The findings pointed out that maximum collector efficiency was obtained at inclination angle of 60°. The percentage error between the developed correlation and experimental data was 6% and 8.3% for *Nu* and *f* respectively. Jia et al. [18] performed a study to enhance the thermal performance of the spiral solar air heater (SSAH) incorporated with baffles. Four types of the SSAH; right angle RA-SSAHS, arc spiral SSAH, arc spiral SSAH with rectangular hole and rectangular hole SSAH were considered. A 3D numerical model was developed to examine the effect of the baffles on the systems. The results suggested that right-handed SSAH showed the maximum efficiency as compared to other three systems. Saravanakumar et al. [19] optimized the parameters of arc shaped rib roughened SAH incorporated with fins & baffles. The results indicated that highest exergy efficiency of 5.2% was achieved of at m_a 0.012 kg/s. For highest exergy efficiency, total number of fins used in the system was 8 , baffle length was 0.2 m and baffle width was 0.015 m. Sriromreum et al. [20] examined the impact of baffles on *Nu* in a SAH connected to 45° Z-shaped baffles. They observed a substantial influence of the Z-shaped baffle on *Nu* and *f* of SAH. Tamna et al. [21] analyzed the impact of hindrance promoters on the *Nu* in a STC with $\alpha_a = 45°$ and *Re* ranging from 4000 to 21000. The results show that at P_B/H_B of 0.5 single baffle vortex generator yield the maximum η_p of 1.83. Bekele et al. [22] analyzed the influence of different type of obstructions fixed on a wall having W_D/H_D of 6:1. It was found that η_p of SAH at α_a of 30° and 60° is higher than previous studies. Promvonge and Kwankaomeng [23,24] performed a numerical investigation and determined the Nu_{rs} in a STC with 45° staggered angled baffles and 30° angled baffles. They reported that Nu_{rs} was enhanced about 9.23 times and f_{rs} varies from 1.09 to 45.31 times compare to STC without baffles. Alam et al. [25] analyzed the impact of perforated baffles on Nu_{rs} and f_{rs} for a STC. They found that Nu_{rs} and f_{rs} enhanced 6.76 and 28.84 times as compared to that of smooth STC. Jouybari and Lundstrom [26] experimentally studied the influence of porous media covered on a heated plate of a SAH. They concluded that inclusion of thin, porous layer results in five-fold increase in the TP of a SAH. Sivakandhan et al. [27] used an analytical hybrid duct configuration for HT enhancement of STC. The authors found 22.4% and 18.1% increase in thermal and actual efficiency of modified SAH as compared to conventional SAH. Hassan et al. [28] have made comparison between the performance of conventional STC and roughened STC. The efficiency of roughened STC was found about 83.6%, 76.3% and 59.8% at m_a of 0.075, 0.05 and 0.025 kg/s as compared to conventional STC respectively. Jia et al. [29] examined SAH with the spiral shape of spoiler. They studied influence of temperature variation between entry and exit, irradiance and air volume on performance of SAH. Kumar [30] experimentally investigated Nu_{rs} and f_{rs} of a three-side concave dimple roughened SAH. The author also developed correlations for Nu_{rs} and f_{rs} . Kumar et al. [31] have analyzed the impact of V-pattern baffles on the η_P of STC. Mansoury et al. [32] experimentally examined the performance of sundry parallel flow heat exchangers. The experiment was carried out with distilled water and different concentration of Al_2O_3 in water. Out of different type of heat exchanger used, the double-pipe heat exchanger was found to have best performance. Bashirnezhad et al. [33] investigated thermal conductivities of various nanofluids. The experimentation was done with various types of nanoparticles of Al, Fe, Ti and Cu. Different kinds of base fluids were used during experimentation. Kherbeet et al. [34] analyzed the impact of laminar nanofluid flow on the HT. The experiments were performed with different lengths of microscale-backward/forward facing step. The 30 nm sized SiO_2 nanoparticles immersed in distilled water were used. The microscale forward facing step was found to be yield highest *Nu* . Aramesh et al. [35] investigated effect of nanofluids on the performance of a STC. Nitin et al. [36] analyzed impact of conical ring obstacles on the*Nu and f* of impingement round jets SAH. Authors concluded that the conical ring obstacles SAH with jet impingement is better than smooth SAH. The studies [37–39] examined the improvement in efficiency of a Solar Still, efficiency a solar power plant using heliostat field and exergy-based optimization for STC. The developments in different solar desalination methods, impact of combined AR and highly conductive fluids on performances of STC and Solar flux distribution in heat pipe cavity receiver is examined in studies [40–42]. Menni et al. [43,44] examined hydrodynamic behavior and thermal-aerodynamic characteristics in solar duct roughened with baffles.

From the literature mentioned above it is clear that the artificial roughness outcomes in the enhancement of the thermohydraulic efficiency of the STC. The previous studies on STC roughened with various types of roughness show appreciable heat transfer enhancement but very few studies have utilized angled perforated baffles. As per author knowledge, a comprehensive study on the performance analysis of STC roughened with angled perforated baffles using different techniques is not available. The present work novelty lies in the fact that in addition to the experimental examination of STC performance, correlations for Nu_{rs} and f_{rs} from experimental data are developed and modelling of thermal parameters using CCD and Artificial Neural Network (ANN) have also been performed. To the best of author's knowledge, this type of

Fig. 2. Pictorial view of the experimental arrangement.

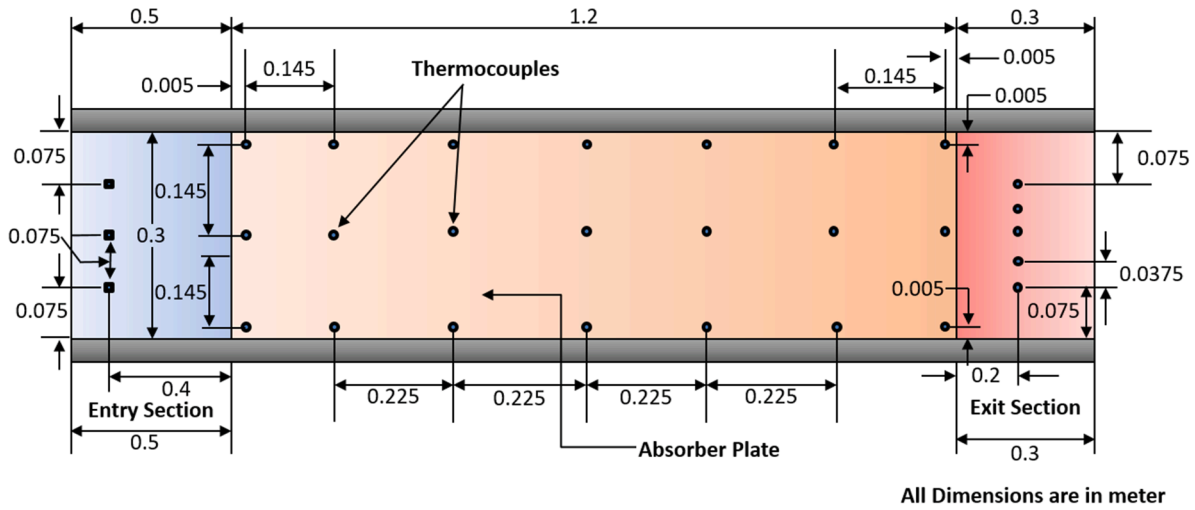

Fig. 3. Location of the thermocouples.

modelling is performed first time for SAC with angled perforated baffles.

Experimental details and roughness parameters

According to the guidelines of the ASHRAE standard [45] an experimental setup is fabricated to analyze the impact of angled perforated baffle on Nu_{rs} and f_{rs} of the STC.

Experimental setup

Fig. 1 represents the schematic representation of experimental set up. Pictorial view of testing apparatus (STC) with digital micro manometer is illustrated in Fig. 2. The internal dimension of the rectangular wooden conduit are $2\,m \times 0.3\,m \times 0.03\,m$. The STC have an inlet section, a test section and outlet section equal to $0.5\,m$, $1.2\,m$ and $0.3\,m$ respectively. Main parts of the test setup include rectangular channel made of wooden, voltmeter, ammeter, orifice plate, electric heater, U-tube manometer, high-pressure blower to transfer air, control valve, micro-manometer, thermocouples, and variable transformer etc. A well-armed nichrome wire electric heater is used to transfer 1000 W/m^2 heat flux over an array of test portions. A variable transformer is employed to control the heat flux. The mica sheet is sandwiched between the nichrome wire and the asbestos sheet to prevent back heating from the heater and thus prevents top loss

To facilitate the heat transfer, a $0.0016\,m$ size GI sheet painted in black is used as a heated wall on the upper side of STC. U tube manometer connected to a calibrated orifice meter is used to flow rate of air through the rectangular channel. The experimental set up is illustrated in the Fig. 2. The flow rate is varied using control valve. Temperature of heated plate and air is recorded using copper-based thermocouples [46]. Twenty-nine thermocouples have been used for measurement of temperature in the rectangular channel as depicted in Fig. 3. A digital micro-manometer is employed to determine the pressure drop. The precision of measuring instruments used in the investigation is listed in Table 1.

Table 1
Precision of measuring instruments.

S.No.	Measurement	Instrument	Precision
1	Dimensions of channel	Vernier caliper	$\pm 0.02mm$
2	Pressure drop across the channel	Micro-manometer	$\pm 0.1Pa$
3	Pressure drop across the orifice-plate	U-tube manometer	$\pm 1mm$
4	Temperature measurement	Thermocouple	$\pm 0.25°C$
5	Orifice plate and throat diameter	Vernier caliper	$\pm 0.02mm$

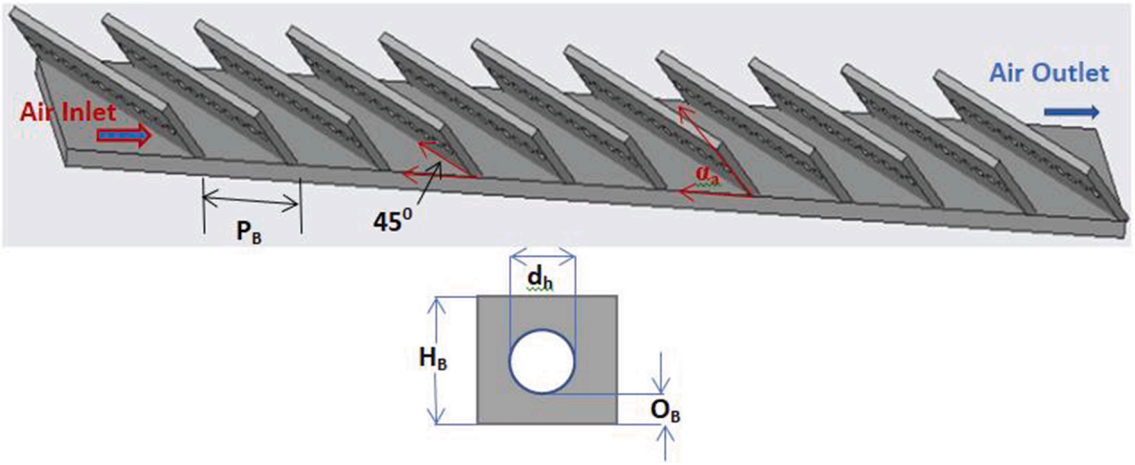

Fig. 4a. Schematic of angled perforated baffles.

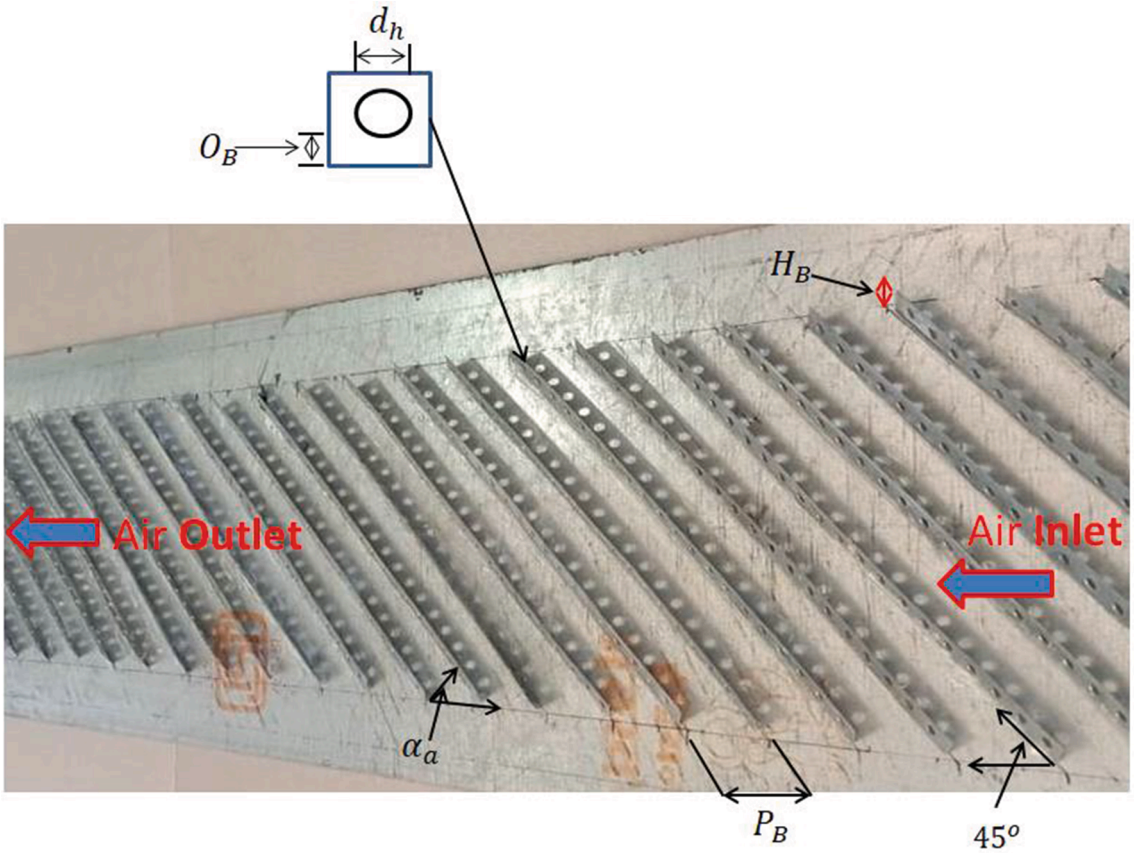

Fig. 4b. Actual view of angled perforated baffles on absorber plate.

Table 2
Range of the perforated angled baffles roughness parameters.

Sr. No.	Operating parameters	Symbols	Range
1.	Channel aspect ratio	W_D/H_D	10 (fixed)
2.	Relative baffle height	H_B/H_D	0.50 (fixed)
3.	Relative baffle pitch ratio	P_B/H_B	10 (fixed)
4.	Relative hole position	O_B/H_B	0.266 (fixed)
5.	Angle of attack	α_a	35°- 65° (7 steps)
6.	Open area ratio	β_0	12%
7.	Reynolds number	Re	5000–17000 (7 steps)

Selection of experimental parameters

The perforated baffles are fixed at different α_a on the absorber plate and tested to examine their impact on Nu_{rs} and f_{rs} . The inclination angle is fixed at 45^0 as shown in the Fig.4 in accordance with past studies. As per past studies [47], the inclination angle of 45^0 provides simple way to secondary stream. The stream has less time on the tested plate to acquire appropriate heat. However large value of inclination is also not good. The larger value of inclination locates the baffles at large angles opposing primary and secondary flow (SF). The large angled position of baffles results in the more special movement of SF and vortices which cause reduction in the strength of flow and heat conveying capacity. The

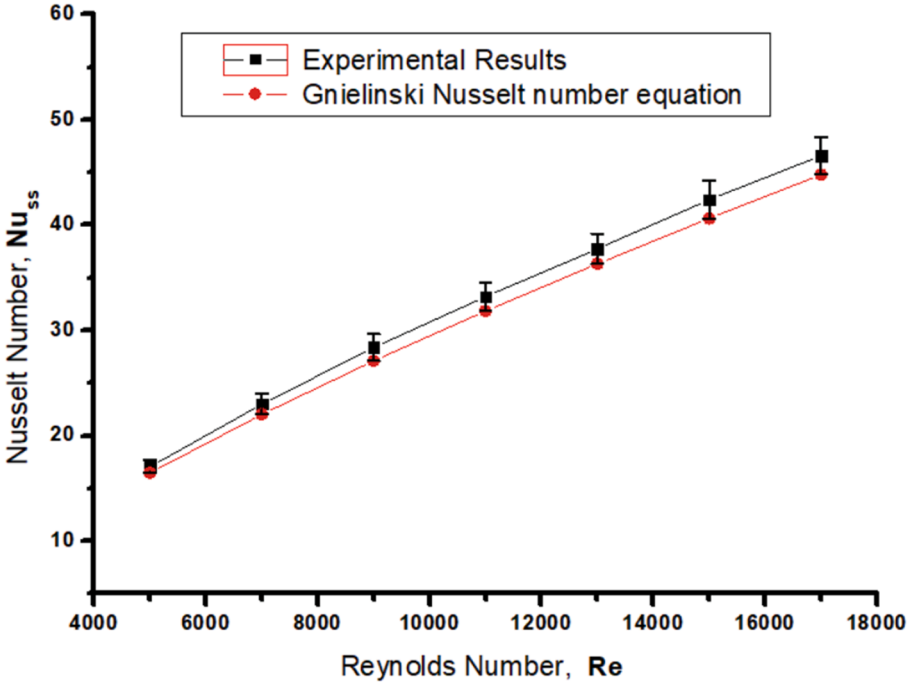

Fig. 5. Evaluation of expected and experimental results of Nu_{ss} for smooth wall.

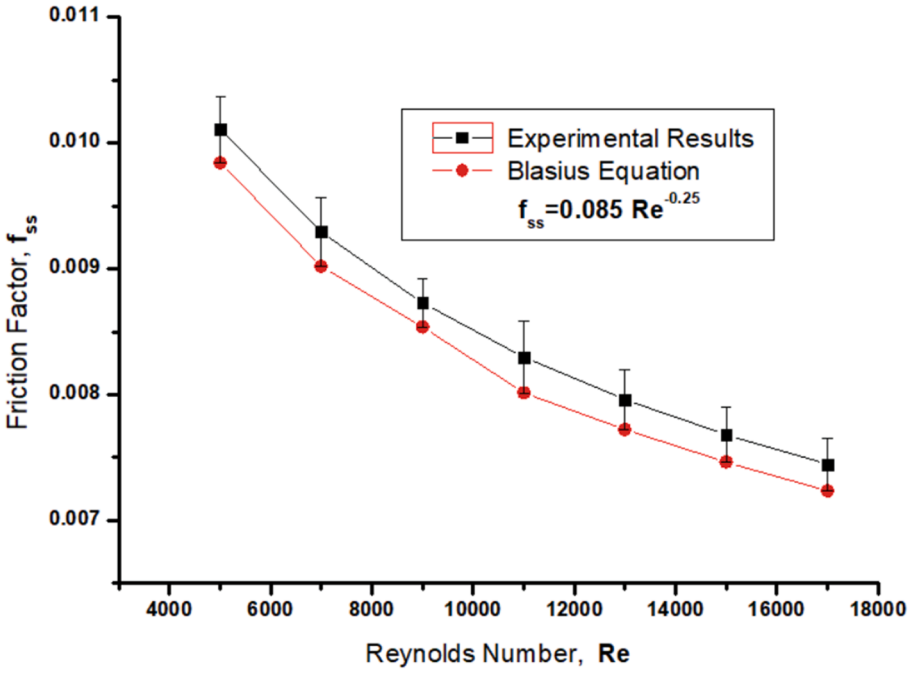

Fig. 6. Evaluation of expected and experimental results of f_{ss} for smooth wall.

channel size; channel length (L_c) of 2 m , channel width (W_D) of 0.3 m and channel height (H_D) of 0.03 m , has been specifically chosen based on previous studies. The geometry of angled perforated baffle is defined with angle of attack (α_a), baffle height (H_B) , hole position from baffle base (O_B) , pitch of baffle channel (P_B) and length of angled pattern baffle (L_v) . To select the precise roughness geometry for STC, α_a is varied and the rest of the geometric parameters i.e. relative baffle height (H_B/H_D) , relative baffle pitch ratio (P_B/H_B) , relative hole position (O_B/H_B) , channel aspect ratio (W_D/H_D) and open area ratio (β_0) are kept constant. The schematic and actual diagram of angled perforated baffles selected for experiments has been illustrated in Figs. 4(a) & 4(b). Different parametric range of the angled perforated baffles is listed in Table 2.

Data reduction & validation

The T_p , T_f , m_a , V , D_{hd} , Re , f_{rs} , Q_u , h_t and Nu_{rs} have been determined from experimental observations using different equations [48–50] as discussed in section 3.1. To check the consistency between the present experimental findings and outcomes of previous studies, the experiments are conducted on the test set up. A validity test is executed on the innovative arrangement using a smooth plate prior to perform

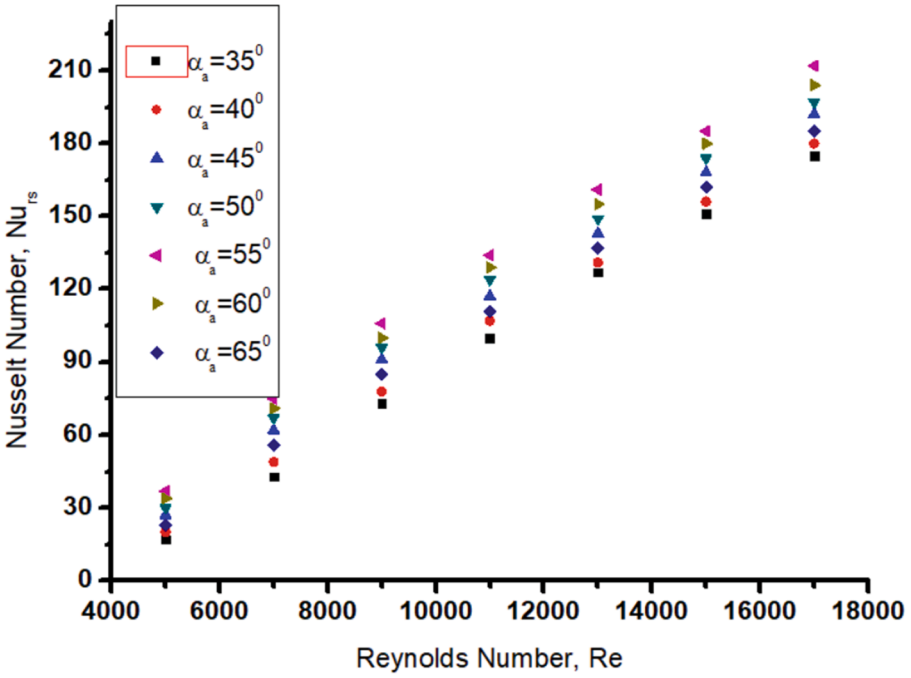

Fig. 7. Variation of Nu_{rs} with Re at selected values of α_a.

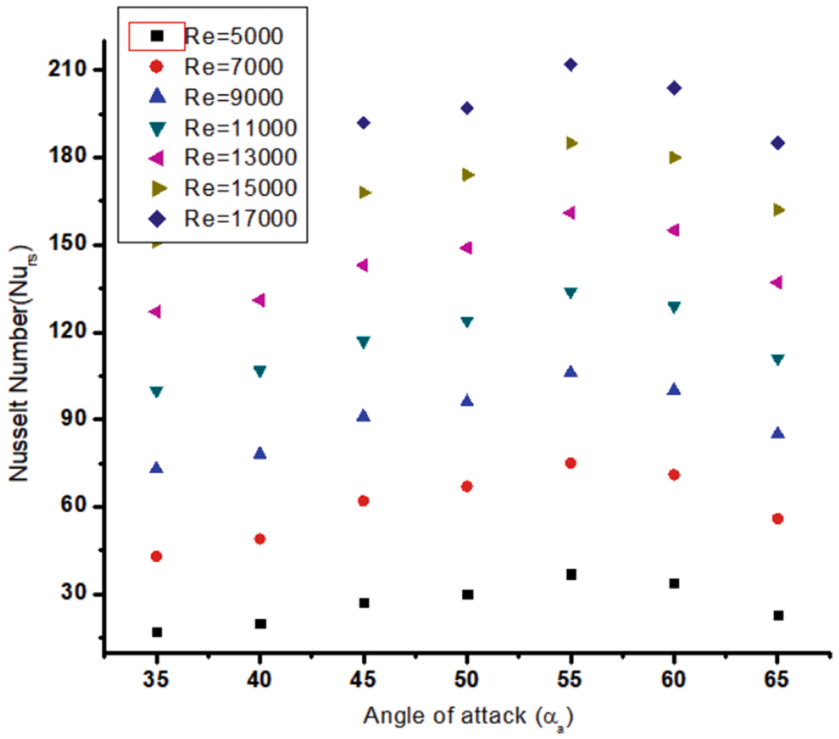

Fig. 8. Variation of Nu_{rs} with α_a at selected values of Re.

experiments on a roughened absorber plate. The findings of the validity test using smooth plate are compared with earlier established correlation of Nu_{ss} and f_{ss} by Gnielinski [15,51] and modified Blasius [52] respectively.

Data reduction

The equations used for the computation of T_p , T_f , m_a , V , D_{hd} , Re , f_{rs} , Q_u , h_t and Nu_{rs} are as follows [48–50]:

1) Mean absorber plate temperature ,

$$T_p = \sum \frac{T_{Pi}}{N} \tag{1}$$

2) Average temperature of the air

$$T_f = \frac{T_i + T_0}{2} \tag{2}$$

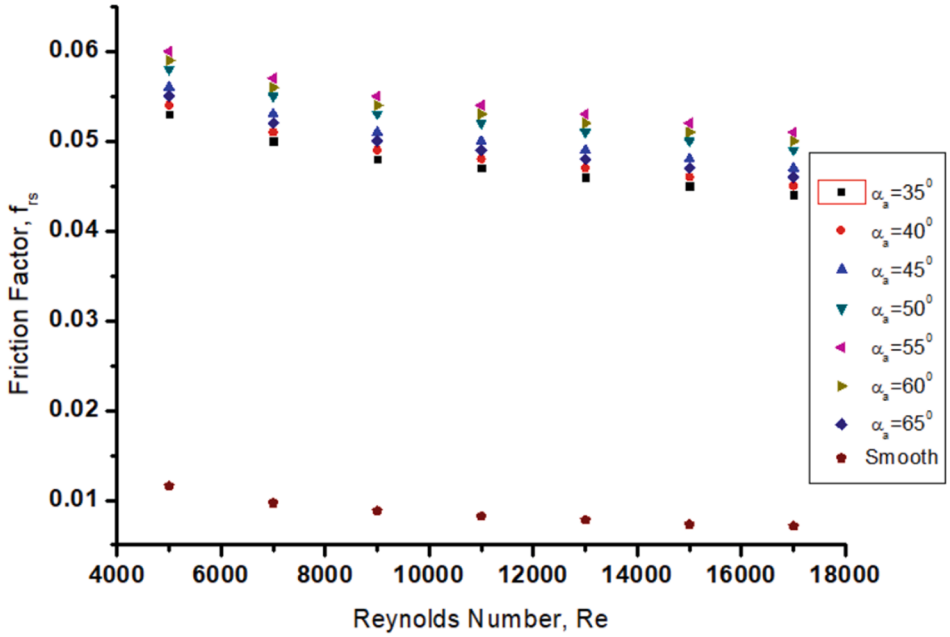

Fig. 9. Variation of f_{rs} with Re at selected values of α_a.

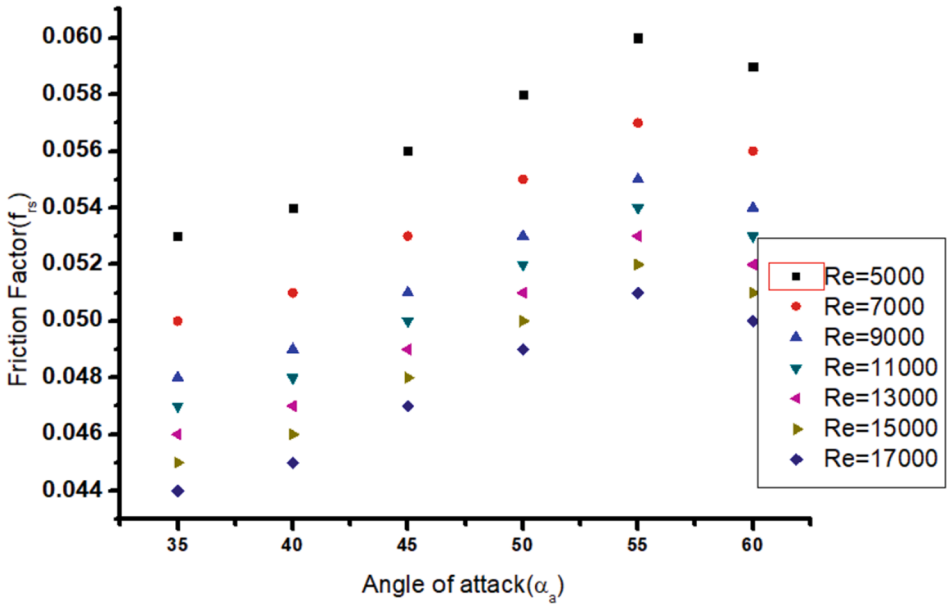

Fig. 10. Variation of f_{rs} with α_a at selected values of Re.

where

$T_0 = (T_{A2} + T_{A3} + T_{A4} + T_{A5} + T_{A6})/5, T_i = T_{A1}$

3) Mass flow rate;

$$m_a = C_{d0} \times A_0 \left[\frac{2 \times \rho_a \times (\Delta P)_0}{1 - \beta_R^{\ 4}}\right]^{0.5} \quad (3)$$

where $(\Delta P)_0 = 9.81 \times \rho_a \times \Delta h_0$

4) Air velocity through channel;

$$V = \frac{m_a}{\rho_a \times W_D \times H_D} \quad (4)$$

5) Equivalent hydraulic diameter;

$$D_{hd} = \frac{4 \times (W_D \times H_D)}{2 \times (W_D + H_D)} \quad (5)$$

6) Reynolds number;

$$Re = \frac{V \times D_{hd}}{\upsilon_a} \quad (6)$$

7) Friction factor

$$f_{rs} = \frac{2 \times (\Delta_p)_d \times D_{hd}}{4 \times \rho_a \times L_t \times V^2} \quad (7)$$

$$(\Delta_p)_d = 9.81 \times \Delta h_0 \times D_{hd} \times \rho_a \times m_a$$

8) Useful energy gain

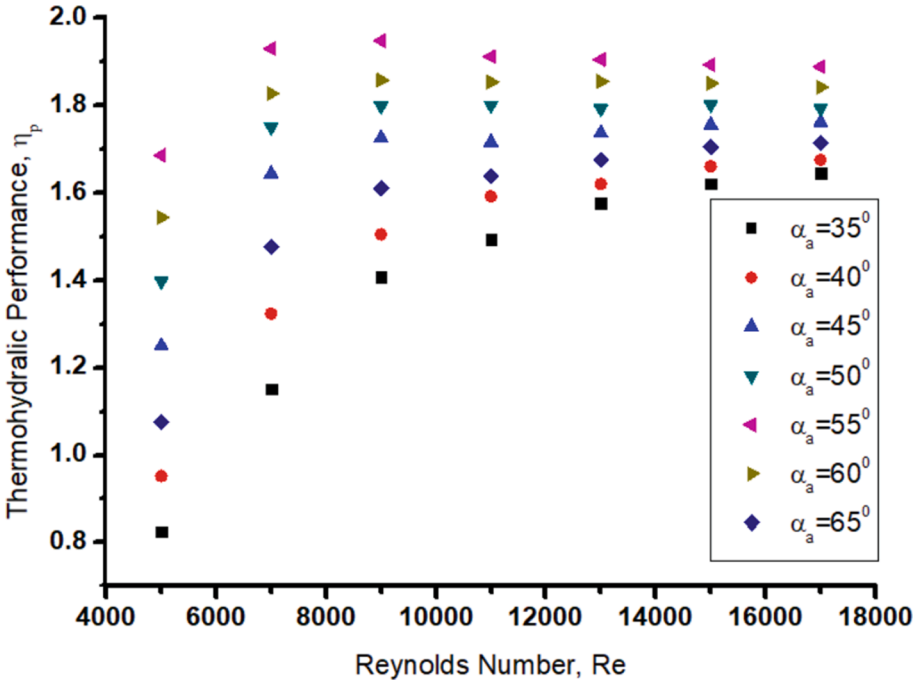

Fig. 11a. Variation of η_p with *Re* at selected values of α_a.

Table 3
Comparison of Thermohydraulic performance of present work with similar previous studies.

S. No.	Study	Geometrical parameters considered	Thermo-hydraulic performance
1	Sharma et al. [62]	Six different baffles viz. Transverse, inclined transverse, dimple, inclined dimple, arc and sine wave	1.22–2.05
2	Pandey et al. [63]	Study Perforated V-down baffle (racetrack shaped holes with staggered openings)	1.12–1.435
3	Chamoli & Thakur [64]	Perforated V-down baffle (circular holes)	1.14–1.18
4	Present study	angled perforated baffles	1.63–1.94

$$Q_u = m_a \times C_p \times (T_0 - T_i) \tag{8}$$

9) Heat transfer coefficient

$$h_t = \frac{Q_u}{A_p \times (T_p - T_f)} \tag{9}$$

10) Nusselt Number

$$Nu_{rs} = \frac{h_t \times D_{hd}}{K_a} \tag{10}$$

Because of existence of the random errors, the actual outcomes deviate from the experimental outcomes. The random errors give rise to the probable uncertainties. So the determination of these uncertainties in the examined results become essential [53]. Uncertainties associated with measured quantities are computed and listed in the Appendix-1 as Table-A1.

Data validation

To check the consistency between the present experimental findings and outcomes of previous studies, the experiments are conducted on the test set up. For optimization of HT rate it is essential to execute a validity test of the innovative arrangement using a smooth plate prior to perform experiments on a rough absorber plate. The findings of the validity test using smooth plate have been listed independently. The results obtained from the validity test of Nu_{ss} and f_{ss} are then compared with well-established correlation for Nu_{ss} and f_{ss} by Gnielinsky [15,51] and modified Blasius [52]. The Gnielinsky equation used to calculate Nu_{ss} and modified Blasius equation used to calculate f_{ss} is given below in equations 11(a) and 11(b).

Gnielinsky equation for Nu_{ss}

$$Nu_{ss} = \frac{\frac{f_s}{8}(Re - 1000)Pr}{1 + 12.7\left(\sqrt{\frac{f_s}{8}}\right)(Pr^{2/3} - 1)} \tag{11(a)}$$

where $f_s = [0.7904\ln(Re) - 1.64]^{-2}$, $3000 < Re < 5 \times 10^6$.

Modified Blasius equation:

$$f_{ss} = 0.085Re^{-0.25} \tag{11(b)}$$

Figs. 5 and 6 represents the evaluation of expected and experimental outcomes of Nu_{ss} and f_{ss} as a function of *Re* .

The average deviation of Nu_{ss} obtained for smooth absorber plate experimentally and computed using equation 11(a) is 4.19%. The average deviation of f_{ss} obtained for smooth absorber plate experimentally and computed using equation 11(b) is 2.84%.

Central composite design (CCD)

A CCD is the most commonly used response surface designed experiment. It is a statistical approach for optimizing processing parameters that is based on a multi-variable nonlinear model. CCD's are factorial or fractional factorial designs with center points, augmented with a group of axial points (also called star points) that let us to estimate curvature. CCD's are used to efficiently estimate first- and second-order terms and model a response variable with curvature by adding center and axial points to a previously-done factorial design. Another type of response surface design is Box-Behnken design (BBD) that does not contain an embedded factorial or fractional factorial design. BBD's usually have fewer design points than CCD's, thus, they can't include runs from a factorial experiment. BBD's always have 3 levels per factor, unlike CCD's which can have up to 5. Also unlike CCD's, BBD's never

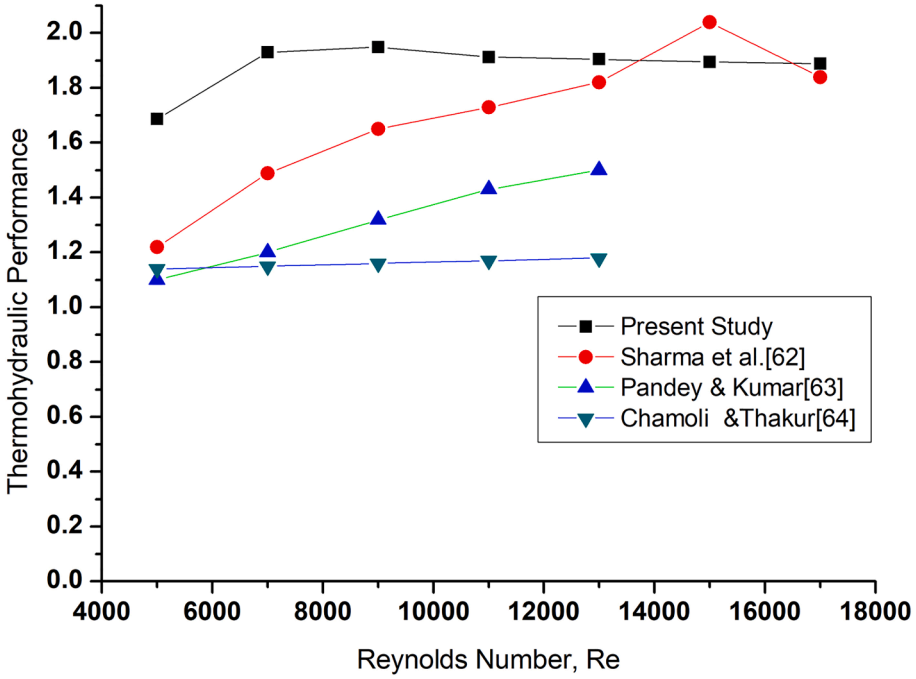

Fig. 11b. Comparative study of present work with similar previous studies.

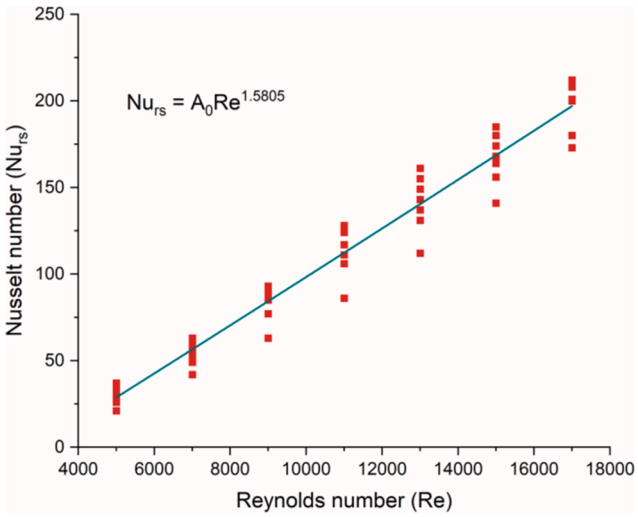

Fig. 12. Plot of Nu_{rs} vs Re.

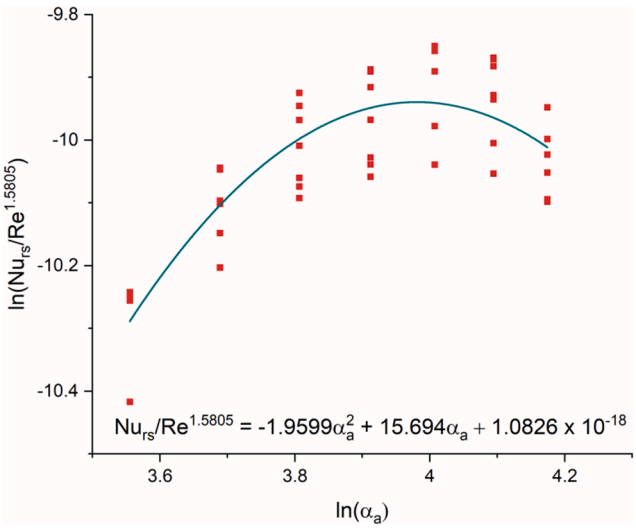

Fig. 13. Plot of $\ln(Nu_{rs}/Re^{1.5805})$ vs $\ln(\alpha_a)$.

include runs where all factors are at their extreme setting, such as all of the low settings. So CCD statistical approach is superior to BBD's statistical approach.

The formulation of regression model equations and operating constraints depending on trials and process parameters is its primary application. The impact of interactions between the various variables that govern the mechanism can be studied using CCD [41]. The CCD was also used to decide the best process variables for the η_P of a solar thermal collector (STC) having an aspect ratio $(W_D/H_D) = 10$. The CCD was applied to a 2nd order quadratic model that needed just a few modelling experiments [54].

The CCD is made up of 2n factor runs (coded in standard notation) and 2n axial runs (±a, 0, 0… 0), (0, ±a, 0, 0… 0)… (0, 0… ±a) and accentor runs. The number of iterations grows as the number of parameters increases. Basically, the optimization process entails three important steps: (1) the prosecution of statistically designed experiments; (2) Coefficient estimation and model adequacy checking in a mathematical model, and (3) the analysis of the results of the experiments [54,55]. In order to investigate the effect of interactions, an analytical model was developed to compare the response to the process variables. It is based on a quadratic model of 2nd order for evaluating various response variables as provided by Eq.12.

$$Y = A_0 + \sum A_1 x_i + + \ + e \tag{12}$$

Where Y is the response variable; A_0 is the intercept; A_i, A_{ij} and A_{ii} are coefficients of linear effect, double interactions; the autonomous variables or factors are xi, xj and e is error.

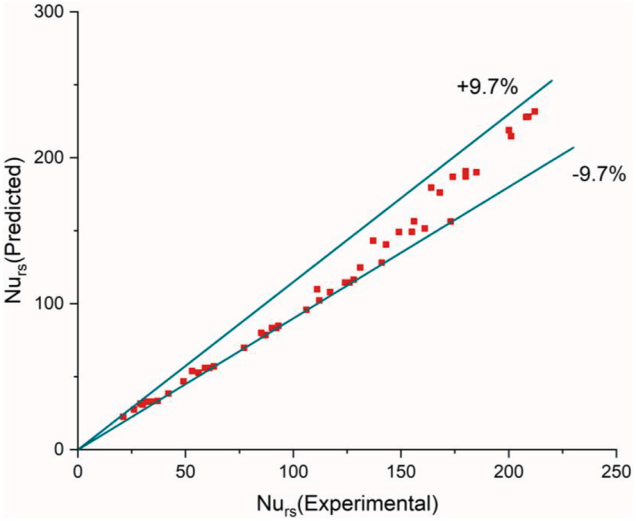

Fig. 14. Plot of estimated results vs experimental results of Nu_{rs}.

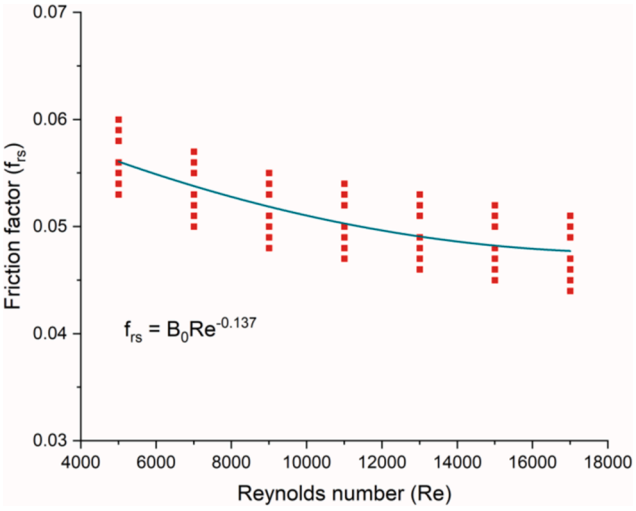

Fig. 15. Plot of f_{rs} vs *Re*.

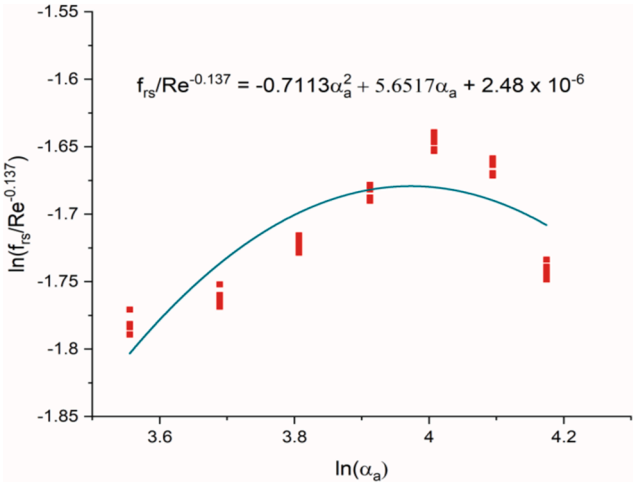

Fig. 16. Plot of $\ln(f_{rs}/\mathrm{Re}^{-0.137})$ vs $\ln(\alpha_a)$.

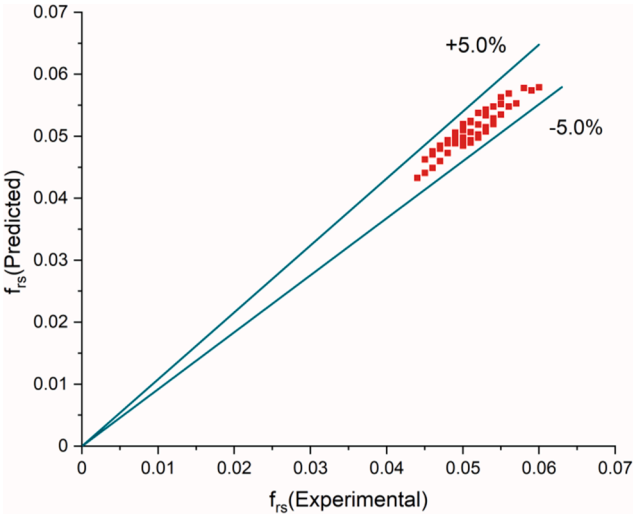

Fig. 17. Plot of estimated results vs experimental results of f_{rs} .

Results and discussion

Heat transfer and fluid flow characteristics

The angled perforated baffles pasted on target plate of an STC generate turbulence in the air flow. Hence there is a generation of vortices in the flow which is responsible for proper mixing and enhancement in Nu_{rs} . Also, the presence of baffles increases the f_{rs} and thus causes the generation of hot regions. This problem was overcome with the help of perforation in the angled baffle. The perforation in the angled baffles permit a portion of stream to enter and travel through holes and therefore warm regions are minimized. This results in the elimination of hot spots and improvement in Nu_{rs} . During experimental analysis, the α_a values are varied from 35° to 65° and optimal results for Nu_{rs} is received at α_a of 55°. This is because at $\alpha_a = 55°$, vortices rush in uppermost end of baffle and get closer to the trailing end. This condition is attributed to a strong spanwise Nu_{rs} , varying of which favor the vortices and a slope to secondary stream. Therefore, it freely mix with mainstream and decreases f_{rs} by a considerable amount.

The current experimental investigation on STC with angled perforated baffle is obtained in the form of Nu_{rs} and f_{rs} . Fig. 7 shows Nu_{rs} variation with *Re* for different values of α_a and rest of the roughness parameters such as $W_D/H_D = 10$, $H_B/H_D = 0.50$, $P_B/H_B = 10$, $O_B/H_B = 0.26$ and $\beta_O = 12\%$ are kept fixed. Fig. 7 shows that Nu_{rs} rises with rise in *Re* as expected. This is because of the increase in turbulent intensity which gives higher Nu_{rs} . The experimental findings reveal rise in Nu_{rs} with increase in α_a . For the different values of α_a taken, Nu_{rs} is found to be maximum at $\alpha_a = 55^o$. This trend is due to the artificial roughness which disrupts the growth of the air flow boundary layer and increases the amount of turbulence. With further rise in the value of α_a , the value of Nu_{rs} begins to reduce. The roughness with $\alpha_a = 55°$ results 3.82 times more enhancement in Nu_{rs} in comparison to smooth surface. Fig. 8 shows Nu_{rs} variation with α_a for selected values of *Re* and other roughness parameters such as $W_D/H_D = 10$, $H_B/H_D = 0.50$, $P_B/H_B = 10$, $O_B/H_B = 0.26$ and $\beta_O = 12\%$ are kept fixed. From the findings, it is concluded that for different values of α_a , Nu_{rs} is highest for the $\alpha_a = 55°$ for all selected *Re* . Fig. 9 represents change in f_{rs} with *Re* at distinct values of α_a and constant values of other roughness parameters. The value of f_{rs} rises with α_a and become maximum at $\alpha_a = 55°$. Further escalation in α_a results in the reduction of f_{rs} . The minima and maxima of f_{rs} are found at $\alpha_a = 35°$ and $\alpha_a = 55°$ respectively. Fig. 10 represents change in f_{rs} with α_a for STC having angled perforated baffles at selected *Re* . It is observed that at different values of α_a , f_{rs} is maximum at $\alpha_a = 55°$ for all selected values of *Re* .

Table 4
Comparison of developed Correlations with previous studies.

S. No	Author	Geometry	Correlation	% Deviation from experimental data
1	Pandey and Kumar [63]	V down baffle blocks	$\eta = 5.20493 \times 10^{-13} \times Re^{6.2677}\left(\frac{e}{H}\right)^{2.6363} \times \left(\frac{P}{e}\right)^{0.066} \times exp\left[-0.3383\{ln(Re)\}^2\right] \times exp\left[2.1057\left\{ln\left(\frac{e}{H}\right)\right\}^2\right] \times exp\left[-0.0544\left\{ln\left(\frac{P}{e}\right)\right\}^2\right]$	The correlations established for 'η' lie in the ±10% deviation range
2	Kumar et al. [65]	discretized broken V-pattern baffle	$Nu_{rs} = 3.766 \times 10^{-5} Re^{0.964}\left(\frac{H_b}{H}\right)^{-0.051}\left(\frac{g_w}{H_b}\right)^{-0.007} exp\left[-0.299\left\{ln\left(\frac{g_w}{H_b}\right)\right\}^2\right]\left(\frac{D_d}{L_V}\right)^{0.227} exp\left[-0.088\left\{ln\left(\frac{D_d}{L_V}\right)\right\}^2\right]\left(\frac{P_b}{H}\right)^{-0.033} exp\left[-0.043\left\{ln\left(\frac{P_b}{H}\right)\right\}^2\right]\left(\frac{\alpha}{60}\right)^{-0.315} exp\left[-0.927\left\{ln\left(\frac{\alpha}{60}\right)\right\}^2\right]$ $f_{rs} = 7.229 \times 10^{-4} Re^{-0.075}\left(\frac{H_b}{H}\right)^{0.024}\left(\frac{g_w}{H_b}\right)^{-0.021} exp\left[-0.191\left\{ln\left(\frac{g_w}{H_b}\right)\right\}^2\right]\left(\frac{D_d}{L_V}\right)^{-0.278} exp\left[-0.243\left\{ln\left(\frac{D_d}{L_V}\right)\right\}^2\right]\left(\frac{P_b}{H}\right)^{-0.024} exp\left[-0.168\left\{ln\left(\frac{P_b}{H}\right)\right\}^2\right]\left(\frac{\alpha}{60}\right)^{-0.145} exp\left[-0.343\left\{ln\left(\frac{\alpha}{60}\right)\right\}^2\right]$	Correlations of Nu_{rs} and f_{rs} with predict experimental results with accuracy of ± 13.5%.
3	Chauhan and Thakur [66]	Smooth absorber plate with jet impingement	$Nu = 1.658 \times 10^{-3} Re^{0.8512}\left(\frac{X}{D_h}\right)^{0.1761}\left(\frac{Y}{D_h}\right)^{0.141}\left(\frac{D_j}{D_h}\right)^{-1.9854} \times exp\left[-0.3498\left\{ln\left(\frac{D_j}{D_h}\right)\right\}^2\right]$ $f = 0.347 Re^{-0.5244}\left(\frac{X}{D_h}\right)^{0.4169}\left(\frac{Y}{D_h}\right)^{0.5321}\left(\frac{D_j}{D_h}\right)^{-1.4848} \times exp\left[-0.2210\left\{ln\left(\frac{D_j}{D_h}\right)\right\}^2\right]$	The correlations established for Nu and f lie in the ± 12% deviation range.
4	Kumar et al. [67]	Square shaped ribs	$Nu = 0.00415 Re^{0.95}\left(\frac{P}{e}\right)^{1.217}\left(\frac{e}{D}\right)^{0.243} \times exp\left[-0.265\left\{ln\left(\frac{P}{e}\right)\right\}^2\right]$ $f = 6.436 Re^{-0.4}\left(\frac{P}{e}\right)^{-1.033}\left(\frac{e}{D}\right)^{0.278} \times exp\left[-0.224\left\{ln\left(\frac{P}{e}\right)\right\}^2\right]$	Correlation of Nu and f with deviation in the range of 12% and 15%, respectively.
5	Ravi and Saini [68]	discrete multi V shaped and staggered rib	$Nu = 3.382 \times 10^{-6} Re^{0.9072}\left(\frac{p'}{p}\right)^{-0.0599} \times exp\left[-0.0613\left\{ln\left(\frac{p'}{p}\right)\right\}^2\right]\left(\frac{r}{e}\right)^{0.255} \times exp\left[-0.0846\left\{ln\left(\frac{r}{e}\right)\right\}^2\right]\left(\frac{W}{w}\right)^{10.17} \times exp\left[-2.677\left\{ln\left(\frac{W}{w}\right)\right\}^2\right]$ $fr = 0.2698 Re^{-0.3152}\left(\frac{p'}{p}\right)^{-0.0754} \times exp\left[-0.0692\left\{ln\left(\frac{p'}{p}\right)\right\}^2\right]\left(\frac{r}{e}\right)^{0.1522} \times exp\left[-0.0126\left\{ln\left(\frac{r}{e}\right)\right\}^2\right]\left(\frac{W}{w}\right)^{1.6948} \times exp\left[-0.3191\left\{ln\left(\frac{W}{w}\right)\right\}^2\right]$	Empirical correlations for Nu and f with 7.98% and 4.37% deviation
6	Present study	Angled Perforated baffles	$Nu_{rs} = 1.0826 \times 10^{-18} \times \mathrm{Re}^{1.5805} \times 15.694\alpha_a \times \exp\left[-1.9599\{\ln(\alpha_a)\}^2\right]$ $f_{rs} = 2.48 \times 10^{-6} \times \mathrm{Re}^{-0.137} \times 5.6517\alpha_a \times \exp\left[-0.7113\{\ln(\alpha_a)\}^2\right]$	The statistical correlations developed for Nu_{rs} and f_{rs} predict findings in a variation of ± 9.7% and ± 5.0%.

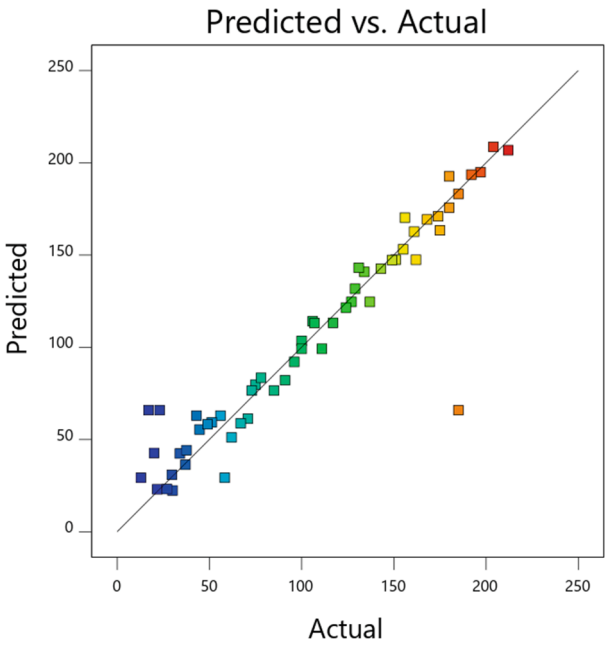

Fig. 18a. Plot of estimated results vs experimental results of Nu_{rs} .

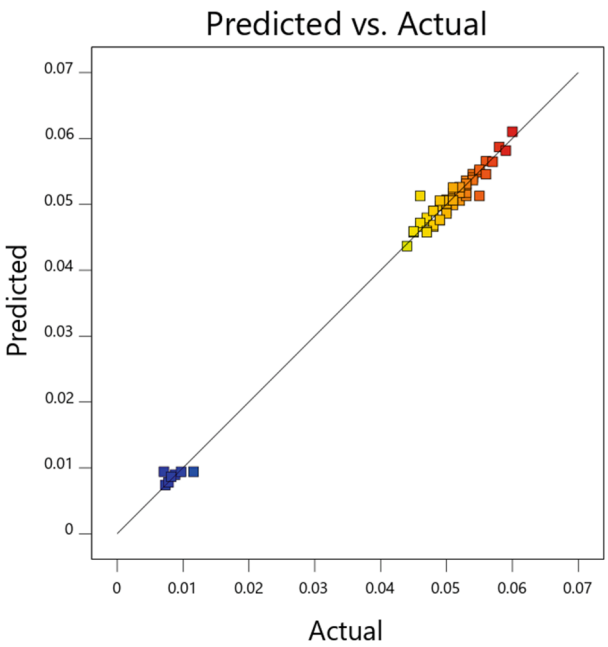

Fig. 18b. Plot of estimated results vs experimental results of f_{rs} .

Thermohydraulic performance

The findings of present study show an increase in Nu_{rs} and f_{rs} using angled perforated baffles. The STC efficiency consequently depends on Nu_{rs}/Nu_{ss} and f_{rs}/f_{ss} . To measure the efficiency of STC, a criterion in the form of η_p is proposed by Lewis [56].The criterion η_p called Thermo-hydraulic parameter (THP) is defined as:

$$\eta_p = (Nu_{rs}/Nu_{ss})/(f_{rs}/f_{ss})^{0.33} \tag{13}$$

Fig. 11 shows the variation of $\eta_p = (Nu_{rs}/Nu_{ss})/(f_{rs}/f_{ss})^{0.33}$ with α_a (35° to 65°) at different values of Re and constant values geometrical factors such as $W_D/H_D = 10$, $H_B/H_D = 0.50$, $P_B/H_B = 10$, $O_B/H_B = 0.44$

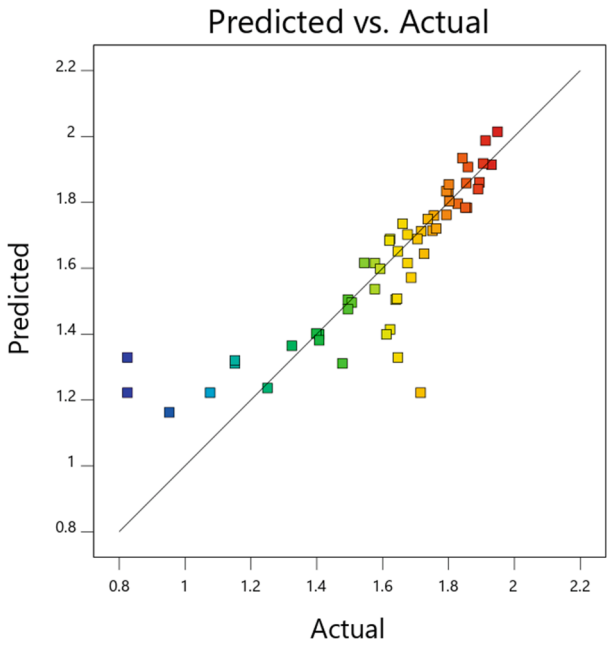

Fig. 18c. Plot of estimated results vs. experimental results of η_p.

and $\beta_O = 12\%$. The inclusion of perforated angled baffles results enrichment in secondary flow streams with increase in α_a is. This causes transmission of heat to the downward flowing air and enhances η_p . Flow in case of perforated angled baffles having $\alpha_a > 55^\circ$ is lean and thus η_p is reduced. The η_p rises with Re up to particular value and then falls as shown in Fig. 11(a). At this value of Re , the STC operates with optimum efficiency. The η_p is basically the ratio of thermo-hydraulic efficiency of STC with perforated angled baffles to that of conventional STC. The $\eta_p < 1$ represents fall in the thermo-hydraulic performance as compared to conventional STC. The $\eta_p < 1$ may be due to small thermal augmentation and more rise of f_{rs} in the STC. In the present work, the obtained value of η_p is 1.94 which represent significant enhancement in the performance of the STC roughened with angled perforated baffles.

Comparative study

The design of STC with roughened baffles is on the basis of maximum HT and minimum f_{rs} . A comparative analysis of the HT augmentation for different geometric parameters is presented in this section based on Nu_{rs} , f_{rs} and η_p . Earlier studies performed by different author's show that the baffles and ribs used as a roughened shape in SAH are considered better for heat transfer compared to other shapes. Istanto et al. [57] used continuous V ribs with different α_a to enhance HT of STC. They reported that the maximum value of $Nu_{rs} = 85$ was obtained with minimum $f_{rs} = 0.08$. Moreover, the value of η_p was obtained to be 1.49 while studying the variation of different α_a on SAH. Lad et al. [58] used inclined ribs and performed a numerical study on SAH. The maximum value of $Nu_{rs} = 75$ was obtained with the corresponding $f_{rs} = 0.042$. They achieved a maximum η_p value of 1.54 for selected range of parameters. Varun et al. [59] performed the study to analyze the performance of SAH roughened with inclined ribs. The augmented value of Nu_{rs} obtained in their study was 60 with a f_{rs} rate of 0.08. Lei et al. [60] explored the impact of angled baffles on HT of heat exchanger and reported a maximum Nu_{rs} of 65 at inclination angle of 45°. Skullong et al. [61] analyzed the behavior of heat transfer with inclined ribs on SAH. The geometric parameters provide highest η_p of 1.12 at lower Re . The maximum value of Nu_{rs} was ranges from 210 to 215 with the minimum f_{rs} rate of 0.044 with perforated baffles. Sharma et al. [62] investigated

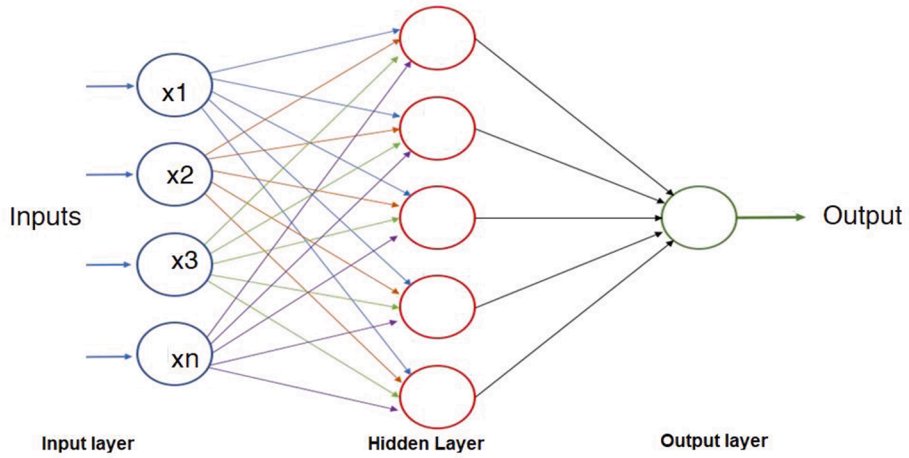

Fig. 19. ANN architecture.

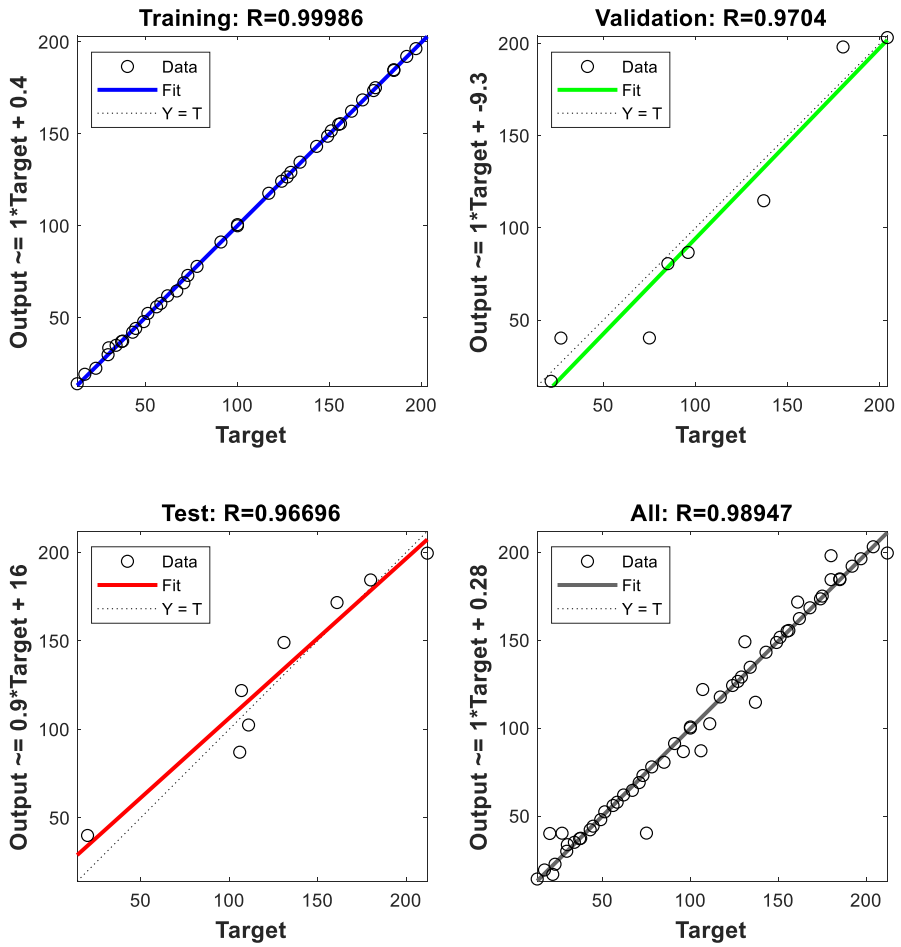

Fig. 20a. Neural network training regression analysis (Optimal performance at 30 neurons in hidden layer Nu_{rs} or f_{rs}.

the η_p of SAH using six dissimilar shaped baffles and compared with CFD simulations. Superlative shape of baffle is selected based on Nu and f . The highest η_p of 2.05 has been obtained with baffle of sine wave shape. Based on operating and geometric parameters the sine wave baffle shape performed superior as compared with other shaped baffles. Pandey & Kumar [63] experimentally examined the impact of V-baffle blocks on the η_p of a rectangular SAH. The outcome shows that STC roughened with V-down baffle gives supreme augmentation of Nu and f over the smooth duct and gives highest η_p of 1.435. Chamoli & Thakur [64] studied effect of perforated baffles in a STC. They found enhancement in Nusselt number using baffle wall in STC. However in the present study angled perforated baffles are used to examine the impact of geometric factors on Nu_{rs} , f_{rs} and η_p . The angled perforated baffles shape provides the larger η_p of 1.94 at α_a of 55° and Re of 9,000. The comparison of present study with similar previous studies is given in Table 3 and plotted in the Fig. 11(b).

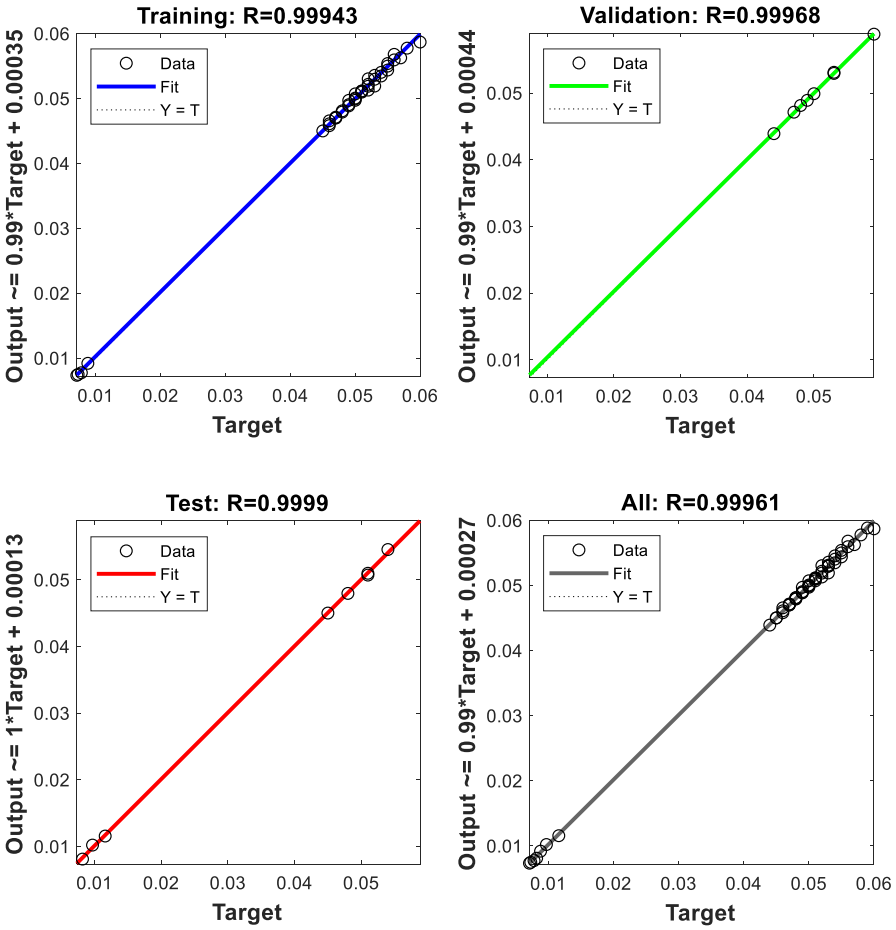

Fig. 20b. Neural network training regression analysis (Optimal performance at 35 neurons in hidden layer for f_{rs}).

Correlation Development for Nu_{rs} and f_{rs}

Correlation for Nu_{rs}

The relative roughened geometric parameters which effectively influence the performance of STC are α_a varied from 35° to 65°, $W_D/H_D = 10$, $H_B/H_D = 0.50$, $P_B/H_B = 10$, $O_B/H_B = 0.44$, $\beta_O = 12\%$. The influence of these dimensionless factors on Nu_{rs} and f_{rs} has been already explained in the results and discussion.

The Nu_{rs} as function of geometrical factors is represented as

$$Nu_{rs} = f_n(Re, W_D/H_D, H_B/H_D, P_B/H_B, O_B/H_B, \alpha_a, \beta_O) \tag{14}$$

The Nu_{rs} calculated from investigational data are plotted against Re and depicted in Fig. 12. A regression analysis was employed to fit the data points into a straight line and achieved relation is specified as follows:

$$Nu_{rs} = A_0 Re^{1.5805} \tag{15}$$

where A_0 is the function of $W_D/H_D, H_B/H_D, P_B/H_B, O_B/H_B, \alpha_a, \beta_O$.

Therefore, $A_0 = Nu_{rs}/Re^{1.5805}$ is plotted against the α_a on $\log_e$ scale as depicted in Fig. 13.

A second order quadratic equation has been fitted during the analysis with the help of regression study and is specified using articulation.

$$\begin{aligned} Nu_{rs}/Re^{1.5805} &= \ln\left(Nu_{rs}/Re^{1.5805}\right) \\ &= -1.9599\alpha_a^2 + 15.694\alpha_a + 1.0826 \times 10^{-18} \end{aligned} \tag{16}$$

By rearranging the equation (16) we will get the correlation for (Nu_{rs}) as:

$$Nu_{rs} = 1.0826 \times 10^{-18} \times Re^{1.5805} \times 15.694\alpha_a \times \exp\left[-1.9599\{\ln(\alpha_a)\}^2\right] \tag{17}$$

Fig. 14 demonstrates a comparison among the experimentally obtained values of Nu_{rs} and empirically calculated values using established correlation (Eq.17). The 96% of experimentally obtained values are within 9.7% deviations. In this way it is inferred the above Nu_{rs} correlation is rationally acceptable for the prediction of Nu_{rs} in STC with perforated angled baffles.

Correlations for f_{rs}

In analogy to the procedure discussed in section 5.1 for the development of correlation for Nu_{rs} , the correlation for f_{rs} is developed.

The functional associations for f_{rs} can be written as:

$$f_{rs} = f_n(Re, W_D/H_D, H_B/H_D, P_B/H_B, O_B/H_B, \alpha_a, \beta_O) \tag{18}$$

All the data of f_{rs} calculated from experimental data are plotted against Re and depicted in Fig. 15. A regression examination is employed

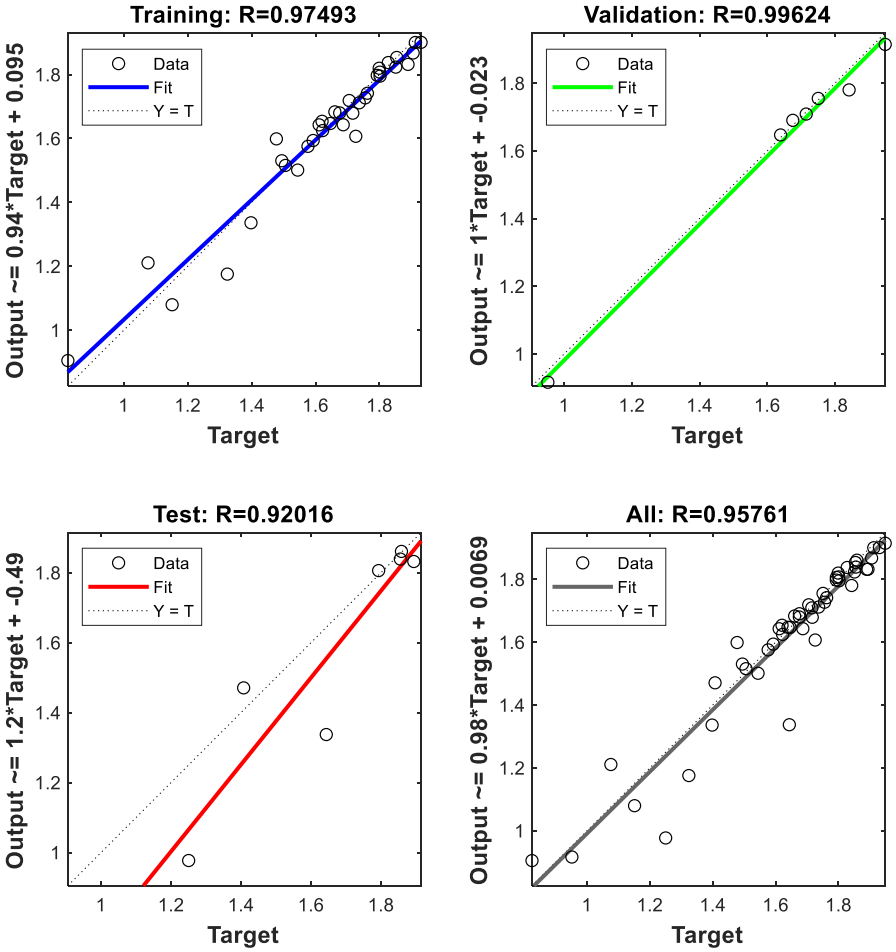

Fig. 20c. Neural network training regression analysis (Optimal performance at 40 neurons in hidden layer for η_p).

to fit the data points into a straight line for information, and the achieved relation is specified as follows

$$f_{rs} = B_0 Re^{-0.137} \tag{19}$$

Here, B_0 is the function of $W_D/H_D, H_B/H_D, P_B/H_B, O_B/H_B, \alpha_a, \beta_O$.

Therefore, $B_0 = f_{rs}/Re^{-0.137}$ is plotted against the α_a on $\log_e$ scale as depicted in Fig. 16. A 2nd order polynomial has been fitted during the analysis with the help of regression study and is specified using articulation

$$f_{rs}/Re^{-0.137} = \ln\left(f_{rs}/Re^{-0.137}\right) = -0.7113\alpha_a^2 + 5.6517\alpha_a + 2.48 \times 10^{-6} \tag{20}$$

By rearranging the equation (20) we will get the correlation for (f_{rs}) as:

$$f_{rs} = 2.48 \times 10^{-6} \times \mathrm{Re}^{-0.137} \times 5.6517\alpha_a \times \exp\left[-0.7113\{\ln(\alpha_a)\}^2\right] \tag{21}$$

Fig. 17 compares the experimentally obtained results of f_{rs} with empirically calculated results using the established correlation as given in Eq. (21). The 96% of experimentally obtained values lies within 5% deviations from empirically calculated values. Hence, the correlation is rationally acceptable for estimation of Nu_{rs} and f_{rs} of the roughened STC with perforated angled baffles in scope of geometrical parameters researched.

Comparison of developed Correlations with previous studies

The developed correlations are compared with correlation developed in similar previous studies as shown in the Table 4.

CCD studies & ANN modelling

Two significant parameters, Reynolds number (Re) and angle of attack (α_a), were proposed in the present study. Subsequently, the independent variables were selected as Re and α_a , while the non-dimensional Nu_{rs} , f_{rs} and η_p was taken as the study's response (dependent variable). As advised by the programme, the final CCD acquired for the non-dimensional Nu_{rs} , f_{rs} and η_p with important terms was linear and is given in Eq. (9).

$$Nu_{rs} = 1.84687 + 0.00695182Re - 5.10845\alpha_a + 0.00115528Re \times \alpha_a \tag{22 a}$$

$$f_{rs} = 0.0259778 + 3.8609e^{-07}Re + 0.00643623\alpha_a - 2.19258e^{-07}Re \times \alpha_a \tag{22b}$$

$$\eta_p = 0.842591 + 4.81292e^{-05}Re + 0.119107\alpha_a - 4.80985e^{-06}Re \times \alpha_a \tag{22c}$$

The actual and values obtained from the correlation is shown in the Figs. 18(a–c) for the non-dimensional Nu_{rs} , f_{rs} and η_p . It can be seen that a good agreement among the predicted and actual findings have been obtained, thus proving efficacy of the proposed CCD modelling [69–74].

The Artificial Neural Network (ANN) is a more advanced method focused on how neurons in the human brain function. Algorithmic models have been generated from the function of these neurons that have been transferred to computing devices. The objective of these algorithms is to produce convergent predictive responses in a wide range of engineering applications. Although the ANN can't match the human

brain's processing speed, it comes very close to empirical, computational, and experimental technological research by mimicking the function of neurons. When opposed to other conventional approaches, the benefits of artificial neural network technique are more associated with linear freedom and broad freedom and nonlinear functional structures.

In this analysis, ANN was used to predict the impact of heat transfer parameters from solar thermal collector (STC) having an aspect ratio $(W_D/H_D) = 10$. Fig. 19 depicts the network structure, which comprises of hidden layers for the input and output parameter. An ANN model was created using the traingdx (feed forward back propagation) training algorithm, learngdm adaptation learning function, and tansig as the transfer function to train the large datasets. MSE was also employed as a performance metric. The stopping criterion for the created ANN model training was "thousand" iteration, "0" error $1e^{-5}$ gradient value, and "thousand" validation error number. Neurons are used to build ANNs, which are made up of three layers: input, intermediary, and output. ANN also has one or more hidden layers. For the neurons, weights and real values are linked. During the training of ANN, in this paper, both input and output quantities were inserted into the framework. By comparing the test outcomes with the output values of the modelled network, the MSE is determined. The weight values between the nodes in the network were modified based on this error statement. The network is trained when the weight values converge. The training algorithm Traingdx has been chosen for this study. For the fourth epoch, the best verification performance was achieved. The network was trained using the data of the experiments. Figs. 20(a–c) depicts the trained network model's training, validation, research, and general regression analyses.

In Fig. 20, the correlation coefficient of ANN models is shown for testing, training, and validation data. The ANN was trained in an iterative manner to reduce the Mean Squared Error (MSE) performance function between the ANN outputs and the target data. It can be shown that ANN modelling with less neurons in the hidden layer correctly estimates the Nu_{rs} and f_{rs} in all cases (with the partial data). Nonetheless, 30 neurons and 40 neurons in the hidden layer framework were employed to simulate the ANN modelling outcome for Nu and FF, respectively, due to the optimal value of the modelling coefficient. The test data is compared to the expected Nu_{rs} and f_{rs} data obtained from ANN. As can be seen, ANN's estimation of the results is significantly better.

Conclusion

In this study, an STC roughened with angled perforated baffle is examined at distinct values of α_a , Re ranges from 5000 to 17,000 and constant roughness parameters such as $W_D/H_D = 10$, $H_B/H_D = 0.50$, $P_B/H_B = 10$, $O_B/H_B = 0.44$ and $\beta_O = 12\%$. Following conclusions are drawn from the findings.

1) The artificial roughness in the form of angled baffles and perforation result substantial improvement in Nu_{rs} and reduction in pressure drop.
2) This improvement in Nu_{rs} is a strong function of α_a and perforation.
3) The Nu_{rs} and f_{rs} of roughened channel with angled perforated baffles improved 3.82 and 7.14 respectively folds in comparison to the channel having no baffles.
4) The use of the angled perforated baffles at $\alpha_a = 55^\circ$ causes high Nu_{rs} and f_{rs} as compared with other values of α_a . The perforated baffles at $\alpha_a = 55^\circ$ provides the larger η_p of 1.94 at Re of 9,000.
5) The statistical correlations developed for Nu_{rs} and f_{rs} in terms of flow parameters and roughness geometries.
6) The developed correlations for Nu_{rs} and f_{rs} predict the experimental findings within a variation of ± 9.7% and ± 5.0% respectively.
7) The CCD is used to decide the best process variables for the η_p of a STC having an aspect ratio (W_D/H_D) of 10. A good prediction of the various output parameters of interest is obtained using ANN for all the thermal characters of SAH.

Future scope of study

In the present study, geometry for optimum performance is selected by testing number of absorber plates roughened with angles perforated baffles. The experimental run and testing of absorber plates consumes material and time. These things are avoided by carrying out this analysis using computational fluid dynamics, which is a possible extension of this work. Beside this, 3E analysis (Energy, exergy and economic) of solar air heater having new design absorber plate with perforated baffle is also a future scope of extension of this work.

CRediT authorship contribution statement

Raj Kumar: Conceptualization, Data curation, Writing – original draft. **Rahul Nadda:** Conceptualization, Validation, Data curation, Writing – original draft. **Sushil Kumar:** Methodology, Validation, Writing – original draft. **Abdul Razak:** Methodology, Validation. **Mohsen Sharifpur:** Supervision, Writing – review & editing. **Hikmet S. Aybar:** Supervision, Writing – review & editing. **C. Ahamed Saleel:** Methodology, Writing – review & editing. **Asif Afzal:** Methodology, Writing – review & editing.

Declaration of Competing Interest

The authors declare that they have no known competing financial interests or personal relationships that could have appeared to influence the work reported in this paper.

Acknowledgment

The authors extend their appreciation to the Deanship of Scientific Research at King Khalid University, Saudi Arabia for funding this work through the Research Group Program under grant no. R.G.P. 2/26/43.

Appendix A1

Sample Calculation for uncertainty analysis

Uncertainty in Area of absorber plate (A_p)

$$A_p = W_D \times L_t$$

$$\frac{\delta A_p}{A_p} = \left[\left(\frac{\delta L_t}{L_t}\right)^2 + \left(\frac{\delta W_D}{W_D}\right)^2\right]^{0.5}$$

$$\frac{\delta A_p}{A_p} = \left[\left(\frac{0.1}{1200}\right)^2 + \left(\frac{0.1}{300}\right)^2\right]^{0.5}$$

$$\frac{\delta A_p}{A_p} = 0.00034359$$

Uncertainty in measurement of Hydraulic diameter (D_{hd})

$$D_{hd} = \frac{4 \times (W_D \times H_D)}{2 \times (W_D + H_D)}$$

$$\delta D_{hd} = \left[\left(\frac{\delta D_{hd}}{\delta W_D} \delta W_D \right)^2 + \left(\frac{\delta D_{hd}}{\delta H_D} \delta H_D \right)^2 \right]^{0.5}$$

$$\frac{\delta D_{hd}}{D_{hd}} = \frac{\left[(1.65289 \times O.1)^2 + (0.0165289 \times 0.1)^2 \right]^{0.5}}{2(300 \times 30)(300 + 30)^{-1}}$$

$$\frac{\delta D_{hd}}{D_{hd}} = 0.0030304246$$

Uncertainty in Area of orifice meter (A_o)

$$A_o = \frac{\pi}{4} {D_o}^2$$

$$\frac{\delta A_o}{A_o} = \frac{\frac{\pi D_o \times \delta D_o}{2}}{\frac{\pi}{4} {D_o}^2} = \frac{2 \times \delta D_o}{D_o} = \frac{2 \times 0.1}{42.96}$$

$$\frac{\delta A_o}{A_o} = 0.0047$$

Uncertainty in density measurement (ρ_a)

$$\rho_a = \frac{P_a}{R \times T_o}$$

$$\frac{\delta \rho_a}{\rho_a} = \left[\left(\frac{\delta P_a}{P_a} \right)^2 + \left(\frac{\delta T_o}{T_o} \right)^2 \right]^{0.5}$$

Taking $P_a = 97500Pa$

$$\frac{\delta \rho_a}{\rho_a} = \left[\left(\frac{0.1}{97500} \right)^2 + \left(\frac{0.1}{25.33} \right)^2 \right]^{0.5} = 3.94 \times 10^{-3}$$

m_a

$$m_a = C_{do} A_o \left[\frac{2 \rho_a (\Delta p)_0}{1 - \beta^4} \right]^{0.5}$$

$$m_a = C_{do} \times A_o \times {\rho_a}^{0.5} \times {(\Delta p)_0}^{0.5} \times \left[\frac{2}{1 - \beta^4} \right]^{0.5}$$

$$\frac{\delta m_a}{m_a} = \left[\left(\frac{\delta C_{do}}{C_{do}} \right)^2 + \left(\frac{\delta A_o}{A_o} \right)^2 + \left(\frac{\delta \rho_a}{\rho_a} \right)^2 + \left(\frac{\delta (\Delta p)_0}{(\Delta p)_0} \right)^2 \right]^{0.5}$$

$$\frac{\delta m_a}{m_a} = \left[\left(\frac{1.5}{100} \right)^2 + (0.0047)^2 + (0.00394)^2 + \left(\frac{0.2}{185} \right)^2 \right]^{0.5} = 0.016241 = 1.6241\%$$Uncertainty in measurement of air velocity in channel (**V**)

$$V = \frac{m_a}{\rho_a \times W_D \times H_D}$$

$$\frac{\delta V}{V} = \left[\left(\frac{\delta m_a}{m_a} \right)^2 + \left(\frac{\delta \rho_a}{\rho_a} \right)^2 + \left(\frac{\delta W_D}{W_D} \right)^2 + \left(\frac{\delta H_D}{H_D} \right)^2 \right]^{0.5}$$

$$\frac{\delta V}{V} = \left[(0.016241)^2 + (0.00394)^2 + \left(\frac{0.1}{300} \right)^2 + \left(\frac{0.1}{30} \right)^2 \right]^{0.5} = 0.017044 = 1.744\%$$

Uncertainty in useful heat gain (Q_u)

$$Q_u = m_a c_p (T_0 - T_i) = m_a c_p \Delta T$$

$$\frac{\delta Q_u}{Q_u} = \left[\left(\frac{\delta m_a}{m_a} \right)^2 + \left(\frac{\delta c_p}{c_p} \right)^2 + \left(\frac{\delta \Delta T}{\Delta T} \right)^2 \right]^{0.5}$$

$$\frac{\delta Q_u}{Q_u} = \left[(0.016241)^2 + \left(\frac{0.1}{1006.141}\right)^2 + \left(\frac{0.1}{5.33}\right)^2\right]^{0.5} = 0.02481 = 2.481\%$$

Uncertainty in heat transfer coefficient (h_t)

$$h_t = \frac{Q_u}{A_p \times (T_p - T_f)} = \frac{Q_u}{A_p \times \Delta T_f}$$

$$\frac{\delta h_t}{h_t} = \left[\left(\frac{\delta Q_u}{Q_u}\right)^2 + \left(\frac{\delta A_p}{A_p}\right)^2 + \left(\frac{\delta \Delta T_f}{\Delta T_f}\right)^2\right]^{0.5}$$

$$\frac{\delta h_t}{h_t} = \left[(0.02481)^2 + (0.00034359)^2 + \left(\frac{0.1}{22.66}\right)^2\right]^{0.5} = 0.0252017 = 2.52\%$$

Uncertainty in Nusselt number (Nu_{rs})

$$Nu_{rs} = \frac{h_t D_{hd}}{K_a}$$

$$\frac{\delta Nu_{rs}}{Nu_{rs}} = \left[\left(\frac{\delta D_{hd}}{D_{hd}}\right)^2 + \left(\frac{\delta h_t}{h_t}\right)^2 + \left(\frac{\delta K_a}{K_a}\right)^2\right]^{0.5}$$

$$\frac{\delta Nu_{rs}}{Nu_{rs}} = \left[(0.0030304246)^2 + (0.0252017)^2 + \left(\frac{0.00001}{0.02529}\right)^2\right]^{0.5} = 0.0394161 = 3.94\%$$

Uncertainty in Reynolds Number (Re)

$$Re = \frac{V.D_{hd}}{\upsilon_a} = \frac{\rho_a V D_{hd}}{\mu}$$

$$\frac{\delta Re}{Re} = \left[\left(\frac{\delta D_{hd}}{D_{hd}}\right)^2 + \left(\frac{\delta V}{V}\right)^2 + \left(\frac{\delta \rho_a}{\rho_a}\right)^2 + \left(\frac{\delta \mu}{\mu}\right)^2\right]^{0.5}$$

$$\frac{\delta Re}{Re} = \left[(0.0030304246)^2 + (0.017044)^2 + (0.00394)^2 + \left(\frac{0.001 \times 10^{-5}}{1.87 \times 10^{-5}}\right)^2\right]^{0.5}$$

$$\frac{\delta Re}{Re} = 0.01776 = 1.77\%$$

Uncertainty in friction factor (f_{rs})

$$f_{rs} = \frac{2(\Delta_p)_d D_{hd}}{4\rho_a L_t V^2}$$

$$\frac{\delta f_{rs}}{f_{rs}} = \left[\left(\frac{\delta D_{hd}}{D_{hd}}\right)^2 + \left(\frac{\delta V}{V}\right)^2 + \left(\frac{\delta L_t}{L_t}\right)^2 + \left(\frac{\delta \rho_a}{\rho_a}\right)^2 + \left(\frac{\delta (\Delta_p)_d}{(\Delta_p)_d}\right)^2\right]^{0.5}$$

$$\frac{\delta f_{rs}}{f_{rs}} = \left[(0.0030304246)^2 + (0.17044)^2 + \left(\frac{0.1}{1200}\right)^2 + (0.00394)^2 + \left(\frac{0.1}{56.2}\right)^2\right]^{0.5}$$

$$\frac{\delta f_{rs}}{f_{rs}} = 0.01784 = 1.784\%$$

Uncertainty in thermohydraulic performance parameter (η_p)

$$\eta_p = (Nu_{rs}/Nu_{ss})/(f_{rs}/f_{ss})^{0.33}$$

$$\frac{\delta \eta_p}{\eta_p} = \left[\left(\frac{\delta Nu_{rs}}{Nu_{rs}}\right)^2 + \left(\frac{\delta f_{rs}}{f_{rs}}\right)^2\right]^{0.5}$$

$$\frac{\delta \eta_p}{\eta_p} = \left[(0.0394161)^2 + (0.01784)^2\right]^{0.5}$$

$$\frac{\delta \eta_p}{\eta_p} = 0.043265 = 4.3265\%$$

The computation of the uncertainties is done for a single set of observation, the uncertainty analysis for all experimental observations is carried out and computed range of uncertainties is listed in Table A1.

Table A1
Uncertainty Range associated with experimental observables.

S. No.	Parameters	Error range, %
1.	Mass flow rate (m_a)	1.532– 2.133
2.	Velocity of air (V)	1.60 – 1.783
3.	Useful heat gain (Q_u)	2.411 – 3.867
4.	Heat transfer coefficient (h_t)	2.164 – 3.421
5.	Nusselt number (Nu_{rs})	3.427 – 4.119
6.	Friction Factor (f_{rs})	1.672 – 2.241
7.	Reynolds Number (Re)	1.56 – 3.27
8.	Thermohydraulic performance parameter (η_p)	3.446 – 5.143

References

[1] Bensaci CE, Moummi A, Flor FJS, Jara EAR, Casado AR, Pardo AR. Numerical and experimental study of the heat transfer and hydraulic performance of solar air heaters with different baffle positions. Renew Energy 2020;155:1231–44.

[2] Kumar R, Nadda R, Rana A, Chauhan R, Chandel SS. Performance investigation of a solar thermal collector provided with air jets impingement on multi V-shaped protrusion ribs absorber plate. Heat Mass Transfer 2020;56(3):913–30.

[3] Mishra PK, Nadda R, Kumar R, Rana A, Sethi M, Ekileski A. Optimization of multiple arcs protrusion obstacle parameters using AHP-TOPSIS approach in an impingement jet solar air passage. Heat Mass Transfer 2018;54(12):3797–808.

[4] Kumar R, Nadda R, Kumar S, Kumar K, Afzal A, Abdul Razak RK, et al. Heat transfer and friction factor correlations for an impinging air jets solar thermal collector with arc ribs on an absorber plate. Sustainable Energy Technol Assess 2021;47:101523. https://doi.org/10.1016/j.seta.2021.101523.

[5] kumar R, Kumar R, Kumar S, Thapa S, Sethi M, Fekete G, et al. Impact of artificial roughness variation on heat transfer and friction characteristics of solar air heating system. Alexandria Eng J 2022;61(1):481–91.

[6] Kumar R, Gaurav, Kumar S, Afzal A, A. Manokar AM, Sharifpur M, Issakhov A, Experimental investigation of impact of the energy storage medium on the thermal performance of double pass solar air heater. Sustainable Energy Technologies and Assessments. Volume 2021;48 :101673.

[7] Khargotra R, Kumar S, Kumar R. Influence of hindrance promoter on the thermal augmentation factor of solar water heater (an experimental study). Renewable Energy 2021;163:1356–69.

[8] Khargotra R, Kumar R, Kumar S. Impact of perforated shapes in delta type hindrance promoter on thermo-hydraulic performance of solar water heating system (An experimental study). Case Stud Thermal Eng 2021;24:100831. https://doi.org/10.1016/j.csite.2020.100831.

[9] Singhy A, Thakur R, Kumar R. Experimental analysis for co-generation of heat and power with convex lens as SOE and linear Fresnel Lens as POE using active water stream. Renewable Energy 2021;163:740–54.

[10] Bhardwaj AK, Kumar R, Kumar S, Goel B, Chauhan R. Energy and exergy analyses of drying medicinal herb in a novel forced convection solar dryer integrated with SHSM and PCM. Sustainable Energy Technol Assess 2021;45:101119. https://doi.org/10.1016/j.seta.2021.101119.

[11] Bhardwaj AK, Kumar R, Chauhan R, Kumar S. Experimental investigation and performance evaluation of a novel solar dryer integrated with a combination of SHS and PCM for drying chilli in the Himalayan region. Thermal Sci Eng Prog 2020;20:100713. https://doi.org/10.1016/j.tsep.2020.100713.

[12] Kashyap K, Thakur R, Kumar S, Kumar R. Identification of Archimedes screw turbine for efficient conversion of traditional water mills (Gharats) into micro hydro-power stations in western Himalayan regions of India: an experimental analysis. Int J Renewable Energy Res 2020;10:1451–63.

[13] Bhatter RK, Abbas A, Rai AK. Effect of Baffles Position on Thermo-Hydraulic Efficiency of a Solar Air Heater. In IOP Conference Series: Materials Science and Engineering. IOP Publishing 2021;1132:012041.

[14] Kumar A, Kim MH. Thermal hydraulic performance in a solar air heater channel with multi-V-type perforated baffles. Energies 2016;9(7):564. https://doi.org/10.3390/en9070564.

[15] Menasria F, Zedairia M, Moummi A. Numerical study of thermohydraulic performance of solar air heater duct equipped with novel continuous rectangular baffles with high aspect ratio. Energy 2017;133:593–608.

[16] Hoonpong P, Skullong S. Performance improvement of solar air heater with V-baffles on absorber plate. J Res Applications Mech Eng 2018;6:29–39.

[17] Luan NT, Phu NM. Thermohydraulic correlations and exergy analysis of a solar air heater duct with inclined baffles. Case Stud Thermal Eng 2020;21:100672. https://doi.org/10.1016/j.csite.2020.100672.

[18] Jia B, Yang L, Zhang L, Liu B, Liu F, Li X. Optimizing structure of baffles on thermal performance of spiral solar air heaters. Sol Energy 2021;224:757–64.

[19] Saravanakumar PT, Somasundaram D, Matheswaran MM. Exergetic investigation and optimization of arc shaped rib roughened solar air heater integrated with fins and baffles. Appl Therm Eng 2020;175:115316. https://doi.org/10.1016/j.applthermaleng.2020.115316.

[20] Sriromreun P, Thianpong C, Promvonge P. Experimental and numerical study on heat transfer enhancement in a channel with Z-shaped baffles. Int Commun Heat Mass Transf 2012;39(7):945–52.

[21] Tamna S, Skullong S, Thianpong C, Promvonge P. Heat transfer behaviors in a solar air heater channel with multiple V-baffle vortex generators. Sol Energy 2014;110:720–35.

[22] Bekele A, Mishra M, Dutta S. Performance characteristics of solar air heater with surface mounted obstacles. Energy Convers Manag 2014;85:603–11.

[23] Promvonge P, Kwankaomeng S. Periodic laminar flow and heat transfer in a channel with 45° staggered V-baffles. Int Commun Heat Mass Transf 2010;37(7):841–9.

[24] Kwankaomeng S, Promvonge P. Numerical prediction on laminar heat transfer in square duct with 30° angled baffle on one wall. Int Commun Heat Mass Transf 2010;37(7):857–66.

[25] Alam T, Saini RP, Saini JS. Experimental investigation on heat transferenhancement due to V-shaped perforated blocks in a rectangular duct of solar air heater. Energy Convers Manag 2014;81:374–83.

[26] Jouybari NF, Lundström TS. Performance improvement of a solar air heater by covering the absorber plate with a thin porous material. Energy 2020;190:116437. https://doi.org/10.1016/j.energy.2019.116437.

[27] Sivakandhan C, Arjunan TV, Matheswaran MM. Thermohydraulic performance enhancement of a new hybrid duct solar air heater with inclined rib roughness. Renew Energy 2020;147:2345–57.

[28] Hassan H, Eifadl SA, Dosoky MFE. An experimental investigation of the performance of new design of solar air heater. Renew Energy 2019;195:89–101.

[29] Jia B, Liu F, Wang D. Experimental study on the performance of spiral solar air heater. Sol Energy 2019;82:16–21.

[30] Kumar V. Nusselt number and friction factor correlations of three sides concave dimple roughened solar air heater. Renew Energy 2019;135:355–77.

[31] Kumar R, Chauhan R, Sethi M, Kumar A. Experimental investigation on overall thermal performance of fluid-flow in a rectangular channel with discrete V-pattern baffle. Therm Sci 2018;22:183–91.

[32] Mansoury D, Ilami Doshmanziari F, Rezaie S, Rashidi MM. Effect of Al2O3/water nanofluid on performance of parallel flow heat exchangers. J Therm Anal Calorim 2019;135(1):625–43.

[33] Bashirnezhad K, Rashidi MM, Yang Z, Bazri S, Yan YM. A comprehensive review of last experimental studies on thermal conductivity of nanofluids. J Therm Anal Calorim 2015;122(2):863–84.

[34] Kherbeet AS, Mohammed HA, Salman BH, Ahmed AE, Alawi OA, Rashidi MM. Experimental study of nanofluid flow and heat transfer over microscale backward- and forward-facing steps. Exp Therm Fluid Sci 2015;65:13–21.

[35] Aramesh M, Pourfayaz F, Haghir M, Kasaeian A, Ahamadi MH. Investigating the effect of using nanofluids on the performance of a double-effect absorption refrigeration cycle combined with a solar collector. Proc Inst Mech Eng, Part A: J Power Energy 2019; 234:981-933.

[36] Kumar N, Kumar A, Maithani R, Thakur R, Kumar R, Thakur A. Effect of circular inside conical ring obstacles on heat transfer and friction characteristics of round jets impingement solar air rectangular passage. Int J Green Energy 2019;16(14):1091–104.

[37] Mandi B, Menni Y, Maouedj R, Lorenzini G, Ahmadi MH, Emani S. Improvement and nocturnal extension of the efficiency of a solar still. Int J Photoenergy Volume 2021 article ID 6631121.

[38] Zolfagharnasab MH, Aghanajafi C, Kavian S, Heydarian N, Ahmadi MH. Novel analysis of second law and irreversibility for a solar power plant using heliostat field and molten salt. Energy Sci Eng 2020;8(11):4136–53.

[39] Grosu L, Mathieu A, Rochelle P, Feidt M, Ahmadi MH, Sadeghzadeh M. Steady state operation exergy-based optimization for solar thermal collectors. Environ Prog Sustainable Energy 2020;39(3). https://doi.org/10.1002/ep.v39.310.1002/ep.13359.

[40] Pourkiaei SM, Ahmadi MH, Ghazvini M, Moosavi S, Pourfayaz F, Kumar R, et al. Status of direct and indirect solar desalination methods: Comprehensive review. Eur Phys J Plus 2021;136(5). https://doi.org/10.1140/epjp/s13360-021-01560-3.

[41] Menni Y, Ghazvini M, Ameur H, Kim M, Ahmadi MH, Sharifpur M. Combination of baffling technique and high-thermal conductivity fluids to enhance the overall performances of solar channels. Eng Comput 2020:1–22.

[42] Jilte R, Ahmadi MH, Kalamkar V, Kumar R. Solar flux distribution study in heat pipe cavity receiver integrated with biomass gasifier. Energy Res 2020;44(9):7698–712.

[43] Menni Y, Ghazvini M, Ameur H, Ahmadi MH, Sharifpur M, Sadeghzadeh. Numerical calculations of the thermal-aerodynamic characteristics in a solar duct

with multiple V-baffles. Engineering Applications of Computational Fluid Mechanics 2020;14(1):1173–97.
[44] Menni Y, Chamkha A, Ameur H, Ahmadi MH. Hydrodynamic Behavior in Solar Oil Heat Exchanger Ducts Fitted with Staggered Baffles and Fins. J. Appl. Comput. Mech., x(x) (20xx) 1-17. doi: 10.22055/JACM.2020.32468.2021.
[45] ASHRAE Standard, Methods of testing to determine the thermal performance of solar collectors, ASHRAE Stand. (2003).
[46] Benedict RP. Fundamental of temperature pressure and stream measurements. third ed. New York: Wiley-Interscience Publication; 1984.
[47] Skullong S. Performance enhancement in a solar air heater duct with inclined ribs mounted on the absorber. Transactions of the TSME 2017;5:55-64.
[48] Hans VS, Gill RS, Singh S. Heat transfer and friction factor correlations for a solar air heater duct roughened artificially with broken arc ribs. Exp Therm Fluid Sci 2017;80:77–89.
[49] Sethi M, Varun, Thakur NS. Correlations for solar air heater duct with dimpled shape roughness elements on absorber plate. Sol Energy 2012;86(9):2852–61.
[50] Gill RS, Hans VS, Saini JS, Singh S. Investigation on performance enhancement due to staggered piece in a broken arc rib roughened solar air heater duct. Renewable Energy 2017;104:148–62.
[51] Thao PB, Truyen DC, Phu NM. CFD analysis and taguchi-based optimization of the thermohydraulic performance of a solar air heater duct baffled on a back plate. Appl. Sci. 2021;11:4645.
[52] Blasius H. Das aehnlichkeitsgesetz bei reibungsvorgängen in flüssigkeiten. In Mitteilungen über Forschungsarbeiten auf dem Gebiete des Ingenieurwesens 1913; 1-41. Springer, Berlin, Heidelberg.
[53] Kline S, McClintock F. Describing uncertainties in single-sample experiments. Mech Eng 1953;75:3–8.
[54] Tamizharasan T, Senthilkumar N, Selvakumar V, Dinesh S. Taguchi's methodology of optimizing turning parameters over chip thickness ratio in machining P/M AMMC. SN Appl Sci 2019;1:160.
[55] Muthuramalingam T, Mohan B. Application of Taguchi-grey multi responses optimization on process parameters in electro erosion. Measurement 2014;58: 495–502.
[56] Lewis MJ. Optimizing the thermohydraulic performance of rough surfaces. Int. J. Heat Mass Transf. 1975;18:1243–8.
[57] Istanto T, Danardono D, Yaningsih I, Wijayanta AT. Experimental study of heat transfer enhancement in solar air heater with different angle of attack of V-down continuous ribs. In: AIP Conf. Proc. 2016;1737:060002.
[58] Lad G, Raghuvanshi N, Mehrotra P, Srivastava A. Numerical investigation of solar air heater duct with square transverse and inclined ribs. Advances in Fluid and Thermal Engineering 2019:445–58.
[59] Varun, Saini RP, Singal SK. Investigation of thermal performance of solar air heater having roughness elements as a combination of inclined and transverse ribs on the absorber plate. Renew Energy 2008;33:1398–405.
[60] Lei YG, He YL, Li R, Gao YF. Effects of baffle inclination angle on flow and heat transfer of a heat exchanger with helical baffles. Chem Eng Process Process Intensif 2008;47(12):2336–45.
[61] Skullong S, Chaidilokpattanakul P, Promvonge P. Effect of inclined ribs on heat transfer behavior in a square channel. International Conference & Utility Exhibition on Power and Energy Systems: Issues and Prospects for Asia (ICUE), Pattaya City, (2011) 1-5.
[62] Sharma S, Das RK, Kulkarni K. Computational and experimental assessment of solar air heater roughened with six different baffles. Case Stud Thermal Eng 2021;27: 101350. https://doi.org/10.1016/j.csite.2021.101350.
[63] Pandey R, Kumar M. Efficiencies assessment of an indoor designed solar air heater characterized by V baffle blocks having staggered racetrack-shaped perforation geometry. Sustainable Energy Technol Assess 2021;47:101362. https://doi.org/10.1016/j.seta.2021.101362.
[64] Chamoli S, Thakur NS. Correlations for solar air heater duct with V-shaped perforated baffles as roughness elements on absorber plate. Int J Sustain Energ. 2016;35(1):1–20.
[65] Kumar R, Chauhan R, Sethi M, Kumar A. Experimental study and correlation development for Nusselt number and friction factor for discretized broken V-pattern baffle solar air channel. Exp Therm Fluid Sci 2017;81:56–75.
[66] Chauhan R, Thakur NS. Heat transfer and friction factor correlations for impinging jet solar air heater. Exp Therm Fluid Sci 2013;44:760–7.
[67] Kumar R, Kumar A, Goel V. Performance improvement and development of correlation for friction factor and heat transfer using computational fluid dynamics for ribbed triangular duct solar air heater. Renewable Energy 2019;131:788–99.
[68] Ravi RK, Saini RP. Nusselt number and friction factor correlations for forced convective type counter flow solar air heater having discrete multi-V shaped and staggered rib roughness on both sides of the absorber plate. Appl Therm Eng 2018; 129:735–46.
[69] Mokashi, Imran, Afzal A, Khan SA, Abdullah NA, Azami MHB, Jilte RD, Samuel OD. Nusselt number analysis from a battery pack cooled by different fluids and multiple back-propagation modelling using feed-forward networks. Int J Thermal Sci 2021; 161:106738.
[70] Afzal A, Saleel CA, Badruddin IA, Khan TY, Kamangar S, Mallick Z, et al. Human thermal comfort in passenger vehicles using an organic phase change material–an experimental investigation, neural network modelling, and optimization. Build Environ 2020;180:107012. https://doi.org/10.1016/j.buildenv.2020.107012.
[71] Ramezanizadeh M, Ahmadi MH, Nazari MA, Sadeghzadeh M, Chen LG. A review on the utilized machine learning approaches for modeling the dynamic viscosity of nanofluids. Renew Sustain Energy Rev 2019;114:109345. https://doi.org/10.1016/j.rser.2019.109345.
[72] Ahmadi MH, Aghaj SSG, Nazeri A. Prediction of power in solar stirling heat engine by using neural network based on hybrid genetic algorithm and particle swarm optimization. Neural Comput Appl 2013;22(6):1141–50.
[73] Nasirzadehroshenin F, Sadeghzadeh M, Khadang A, Maddah H, Ahmadi MH, Sakhaeinia H, et al. Modeling of heat transfer performance of carbon nanotube nanofluid in a tube with fixed wall temperature by using ANN-GA. Eur Phys J Plus 2020;135(2). https://doi.org/10.1140/epjp/s13360-020-00208-y.
[74] Sadeghzadeh M, Ahmadi MH, Kahani M, Sakhaeinia H, Chaji H, Chen LG. Smart modeling by using Artificial Intelligent techniques on thermal performance of flat plate solar collector using nanofluid. Energy Sci Eng 2019;7(5):1649–58.